

Pitch-axis supermanoeuvrability in a biomimetic morphing-wing aircraft

Arion Pons^{1,2,*} and Fehmi Cirak³

¹ Institute of Life Sciences, Hebrew University of Jerusalem, Giv'at Ram, Jerusalem, Israel.

² School of Computer Science and Engineering, Hebrew University of Jerusalem, Giv'at Ram, Jerusalem, Israel.

³ Department of Engineering, University of Cambridge, Cambridge CB2 1PZ, UK

Abstract

Birds and bats are extraordinarily adept flyers: whether in hunting prey, or evading predators, their agility and manoeuvrability in flight are characteristics of vital importance. Their performance, in this regard, greatly exceeds that of conventional aircraft. Attempts to close this gap in capability have typically focused on thrust-vectoring technology – the domain of classical supermanoeuvrability – at the expense of biomimicry. In this work, however, we show that these approaches are not incompatible: biomimetic wing morphing is an avenue both to classical supermanoeuvrability, and to new forms of biologically-inspired supermanoeuvrability. Using a state-of-the-art flight simulator, equipped with a multibody model of lifting surface motion and a Goman-Khrabrov dynamic stall model for all lifting surfaces, we demonstrate the capability of a biomimetic morphing-wing unmanned aerial vehicles (UAV) for two key forms of supermanoeuvrability: the Pugachev cobra, and ballistic transition. Conclusions are drawn as to the mechanism by which these manoeuvres can be performed, and their feasibility in practical biomimetic unmanned aerial vehicle (UAV). These conclusions have wide relevance to both the design of supermanoeuvrable UAVs, and the study of biological flight dynamics across multiple species.

Keywords: supermanoeuvrability, avian flight, biomimetic aircraft, morphing-wing, UAV

1. Introduction

It is evident that birds, bats and other flying creatures show manoeuvrability far beyond the performance of conventional unmanned aerial vehicles (UAVs) of comparable scale. Manoeuvres such as perching [1–3], stall turns [4–7], whiffling [8–10], zero-air-speed rolling

* Corresponding author. *E-mail:* arion.pons@mail.huji.ac.il

[11] and ballistic braking [12,13] all defy the performance limits of conventional aircraft. Many natural flying creatures could indeed be characterized as *supermanoeuvrable*, as per by Herbst [14] and Gal-Or [15]: showing controlled manoeuvrability at angles-of-attack up to 70°, and post-stall capability, and rapid-nose-pointing-and-shooting (RaNPAS) capability. The first supermanoeuvrable aircraft, however, derived inspiration not from biology but from advances in the study of unstable airframes. In the late 1970s the Sukhoi Su-27 carried out the *Pugachev Cobra*, consisting of a rapid pitch-up motion to beyond stall and then down again [16]. This ability was achieved simply by structural and aerodynamic design – large wing strake, nose chines, and an unstable airframe [16–19]. Within a decade supermanoeuvrable aircraft were fast acquiring more capability, primarily due to the key introduction of vectored propulsion [16]. Thrust vectoring is now a standard mechanism via which supermanoeuvrability is achieved, and is a feature of many recent high-performance jet aircraft, including the Mitsubishi X-2 Shinshin [20] and Lockheed Martin F-22 Raptor [17].

Yet the problem and potential of biomimetic supermanoeuvrability remains. Much research has gone into biomimetic UAV design, with a particular emphasis on flapping-wing flight as a propulsive mechanism [21–23]. The scope for biomimicry is vast: among the vertebrate-inspired ornithopters alone there are mimetic seagulls [21], pigeons [24,25], other birds [26–28], bats [29–31], and pterosaurs [32]. At small spatial scales, it is possible to conceive of a biological mechanism of supermanoeuvrability that is analogous to conventional thrust vectoring: the vectoring of flapping-wing thrust via the alteration of wingbeat kinematics. At larger spatial scales, however, other evidence suggests that the mechanisms of flapping-wing propulsion and supermanoeuvrability are not necessarily identical. For instance, flying squirrels, which are without any form of aerial propulsion, show capability for supermanoeuvres such as stall turning and ballistic braking [33–36]. Several species of birds can carry out zero-air-speed rolling and perching manoeuvres without flapping motion [1,11], and perform other manoeuvres such as stall turning in timescales under a single wingbeat cycle [37]. Aldridge [38] concluded from a lift coefficient analysis that several species of bats turn without beating their wings, and evolutionary studies indicate that in the lineage of birds, flight manoeuvrability evolved before a strong power stroke [39].

A pertinent question is thus whether biological and/or conventional forms of supermanoeuvrability could be achieved in a biomimetic morphing-wing UAV. A deeper understanding of biomimetic mechanisms of supermanoeuvrability would not only elucidate

the mechanisms of animal flight, but would have significant implications for the development of artificially-intelligent UAVs for dogfighting [40–42]: indicating that dogfighting UAVs of this form could be developed using a biomimetic morphing-wing platform. In this study, we will explore the potential of a biomimetic morphing-/moving-wing UAV for RaNPAS supermanoeuvrability, with the Pugachev Cobra, alongside its extensions and variations, serving as a primary test manoeuvre. As a case study, we will study a biomimetic morphing-wing UAV, of scale $c.$ 1 m, and equipped with both a conventional propulsion system, and six degree-of-freedom (6-DOF) wing rotation control (asymmetric sweep, dihedral and incidence). We will demonstrate, for the first time, that a system of this form is capable of classical and biomimetic forms of supermanoeuvrability: not only RaNPAS, in multiple forms, but also manoeuvres derived directly from biological behaviour. Wing morphing allows these manoeuvres to be performed in a UAV which is flight-dynamically stable at the level-flight position; and which is equipped with a thrust-to-weight ratio of only 0.5. These results show conclusively that wing morphing is an avenue to supermanoeuvrability, and have implications for both for the design of biomimetic aircraft, and the study of the post-stall flight dynamics of natural creatures.

2. Flight dynamic modelling

2.1. Biomimetic system specification

The target scale for our study of supermanoeuvrability in biomimetic morphing-wing UAV is $c.$ 1 m: approximately equivalent to a range of biological flying creatures, and existing morphing-wing UAVs. Airframe parameters are presented in Table 1, and a scale rendering in Fig. 1, with active morphing degrees of freedom indicated. Figure 1 also illustrates a hypothetical RaNPAS manoeuvre in this system, with applications in air-to-air combat, *cf.* Gal-Or [4]. Several points should be noted regarding these airframe parameters. **(i)** The system wing mass is relatively large, to account for wing strengthening to allow high-incidence states. **(ii)** Lifting surface chords are relatively small, so as to generate an aerodynamically suboptimal system that will represent a conservative model of the capability of a real biomimetic morphing-wing UAV. **(iii)** The 6-DOF morphing configuration is a maximally-actuated state, for scoping purposes – in the course of the analysis, we will identify which of these degrees of freedom are relevant to the particular manoeuvre under consideration.

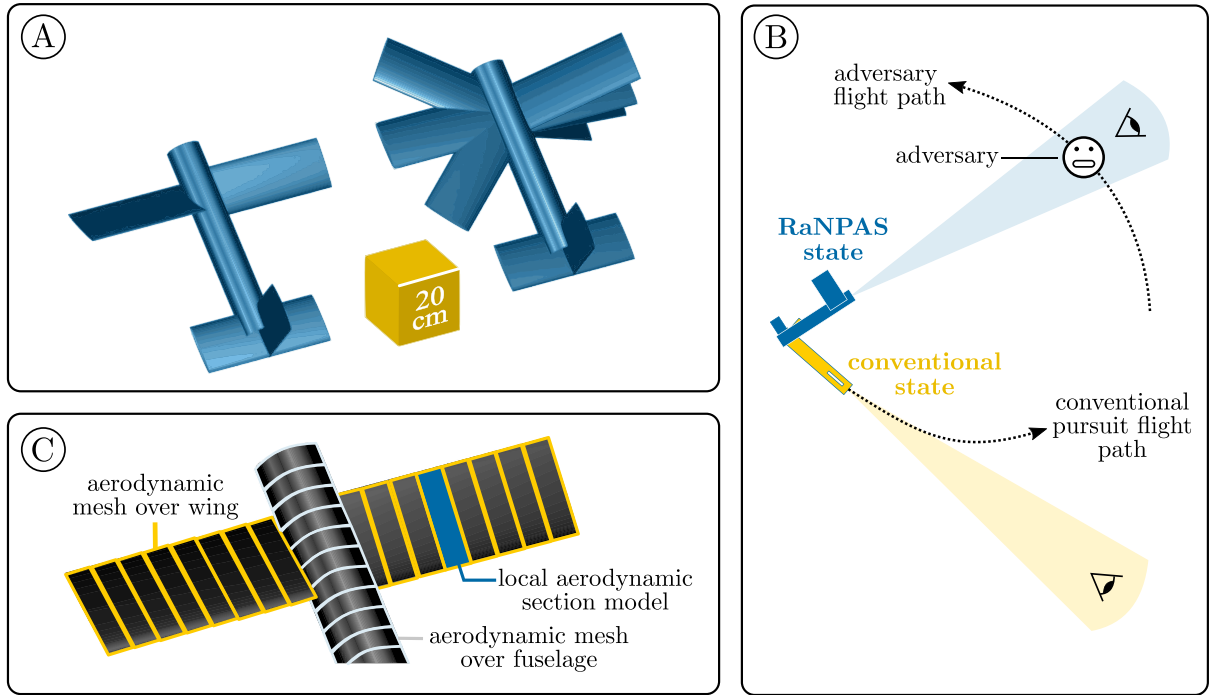


Figure 1: Illustration of the case study biomimetic morphing-wing UAV. (A) Morphing degrees of freedom of the case study system: wing incidence, sweep, and dihedral, all independently controllable on both wings. (B) Dogfighting context of a RaNPAS manoeuvre: the ability to significantly alter the UAV field of view, independent of the flight path. (C) Surface-element modelling context for the case study UAV: an illustrated aerodynamic mesh.

2.2. Flight dynamic modelling framework

The multibody flight dynamic model for the system presented in Section 2.1 is complex. Details are presented in the Supplementary material: here, it is most important to note that, under the assumption of ideal wing actuation dynamics, the UAV flight dynamics permit the 12-DOF nonlinear state-space representation:

$$B_1(\mathbf{z}, \mathbf{v})\dot{\mathbf{z}} = \mathbf{f}(\mathbf{z}, \mathbf{v}) - B_0(\mathbf{z}, \mathbf{v})\mathbf{z}, \quad (1)$$

with a set of N structural and control parameters $\mathbf{v} \in \mathbb{R}^N$, and a state variable $\mathbf{z} \in \mathbb{R}^{12}$ which encodes the reference rotational and translational positions and velocities of the system. Rotational positions are encoded in Euler angles: the gimbal lock problem at the Euler angle pole was bypassed through a pole-switching routine, in which two alternate Euler angle parameterizations were used to maintain non-singularity over the complete orientation space. Within this dynamic model, an aerodynamic section model framework was used to calculate aerodynamic force profiles over each body (lifting surface and bluff), to contribute to the appropriate generalized forces on the system. As part of this process, a local aerodynamic model is used to relate local section flow properties to the section aerodynamic coefficients

and thus forces. The dependency of the system multibody dynamic model (Eq. 12) on this local aerodynamic model may be represented as:

$$B_1(\mathbf{z}, \mathbf{u}, \mathcal{Q}_A(\mathbf{z}, \mathbf{u}))\dot{\mathbf{z}} = \mathbf{f}(\mathbf{z}, \mathbf{u}, \mathcal{Q}_A(\mathbf{z}, \mathbf{u})) - B_0(\mathbf{z}, \mathbf{u}, \mathcal{Q}_A(\mathbf{z}, \mathbf{u}))\mathbf{z}, \quad (2)$$

with the model $\mathcal{Q}_A(\mathbf{z}, \mathbf{u})$ representing the local aerodynamic model and its dependency on structural (\mathbf{u}) and dynamic state (\mathbf{z}) variables.

Table 1: Hybrid system properties with comparisons: n/a, and n/spec denote data not available and not relevant to be specified, respectively.

	This study	NextGen MFX-1 [43]	ShowTime 50 [44]	Greylag Goose (<i>A. Anser</i>) [45–47]
Properties:	Values:			
Length – fuselage	1.20 m	2.1 m	1.51 m	<i>c.</i> 0.82 m
Length – wing to tail	0.80 m	<i>c.</i> 1.17 m	<i>c.</i> 0.94 m	n/a
Length – body radius	0.10 m	<i>c.</i> 0.15 m	<i>c.</i> 0.088 m	n/a
Span – wing	1.60 m	2.8 m	1.46 m	<i>c.</i> 1.62 m
Span – horz. stabilizer	0.80 m	n/a	<i>c.</i> 0.62 m	n/a
Span – vert. stabilizer	0.40 m	n/a	<i>c.</i> 0.17 m	n/a
Chord – wing	0.15 m	<i>c.</i> 0.23	0.32 m	<i>c.</i> 0.26 m
Chord – horz. stabilizer	0.15 m	n/a	<i>c.</i> 0.22 m	n/a
Chord – vert. stabilizer	0.15 m	n/a	<i>c.</i> 0.09 m	n/a
Airfoils	ST50 W/H	n/a	ST50 W/H/V	Complex
Mass – total	8 kg	45 kg	2.9 kg	<i>c.</i> 3.3 kg
Mass – single wing	1 kg	n/a	n/a	n/a
Propulsion – max. thrust	n/spec	<i>c.</i> 200 N	<i>c.</i> 60 N	n/a
Propulsion – mechanism	n/spec	jet engine	propeller	flapping-wing

Previous work [48,49] developed a quasisteady aerodynamic model for $\mathcal{Q}_A(\mathbf{z}, \mathbf{u})$, and validated this model against empirical data for UAV flight dynamics at low levels of aerodynamic unsteadiness. It is clear, however, to model highly-transient RaNPAS behaviour with sufficient accuracy, a quasisteady aerodynamic model is not sufficient. In the context of UAV flight simulation at high levels of flow unsteadiness (local reduced frequency $0.01 < \kappa < 0.5$), higher-fidelity aerodynamic modelling options that have been demonstrated in the literature (i) fully three-dimensional computational fluid dynamics (CFD) simulations [50,51]; (ii) phenomenological dynamic stall and lift hysteresis models, such as the Goman-Khrabrov (GK) [52] model, integrated into the section model framework [3,53–56]; and (iii) model-reduction and machine-learning techniques – including eigensystem realization [57], Volterra theory [58] and support vector machines [59] – applied to higher-fidelity data to generate an accurate lower-order aerodynamic model. In the absence of high-fidelity experimental and computational data for this UAV, we utilize a GK dynamic stall model, accounting for strongly

transient effects arising from aerofoil pitching motion. In the case of the Pugachev cobra manoeuvre, with its strong airframe pitching motion, this is anticipated to be the primary mode of aerofoil transience – and, in addition, GK models have been previously utilized in the study of other agile and morphing-wing UAVs [3,53–55].

3. Goman-Khrabrov aerodynamic modelling

3.1. Formulation

To include dynamic stall effects into the case study model, a modified Goman-Khrabrov (GK) model is implemented in the surface-element framework; extending upon existing work [3,52–56]. Under the modified GK model, for each lifting surface station i across the system, the aerodynamic coefficients for force F as a function of effective angle-of-attack, $C_{i,F}(\alpha_i)$, are given by:

$$C_{i,F}(\alpha_i) = p_i C_{i,F,\text{att}}(\alpha_i) + (1 - p_i) C_{i,F,\text{sep}}(\alpha_i), \quad (3)$$

where $C_{i,F,\text{att}}(\alpha_i)$ and $C_{i,F,\text{sep}}(\alpha_i)$ are the aerodynamic coefficient functions for the hypothetical cases of local attached and separated flow respectively. p_i are local dynamic mixing parameters [56], loosely connected to the location of the separation point along the airfoil chord [60,61], and governed by the first-order differential equation:

$$\tau_{1,i} \dot{p}_i(\alpha_i) = p_{0,i}(\alpha_i - \tau_{2,i} \dot{\alpha}_i) - p_i(\alpha_i), \quad (4)$$

where α_i and $\dot{\alpha}_i$ are the local angle of attack and corresponding rate, $\tau_{1,i}$ and $\tau_{2,i}$ are situation- and station-specific delay parameters and $p_{0,i}(\alpha)$ are mixings function representing the transition between attached and unattached flow. It is the identification of the functions $C_{i,F,\text{att}}(\alpha_i)$, $C_{i,F,\text{sep}}(\alpha_i)$ and $p_{0,i}(\alpha_i)$; and the delays $\tau_{1,i}$ and $\tau_{2,i}$ which are crucial in determining the accuracy of the model. Notably, the former three functions are identifiable based only on static aerodynamic coefficient data, when $p_i = p_{0,i}$.

3.2. Wing quasisteady parameter identification

For our wing aerodynamic data [62], we find that traditional approximations for the GK model parameters, based on flat-plate aerofoil models [53,56], are inaccurate. More recent approaches [60,63,64] involve the identification of these model parameters directly from aerodynamic coefficient data from CFD or experiment. In our system, there are several lifting

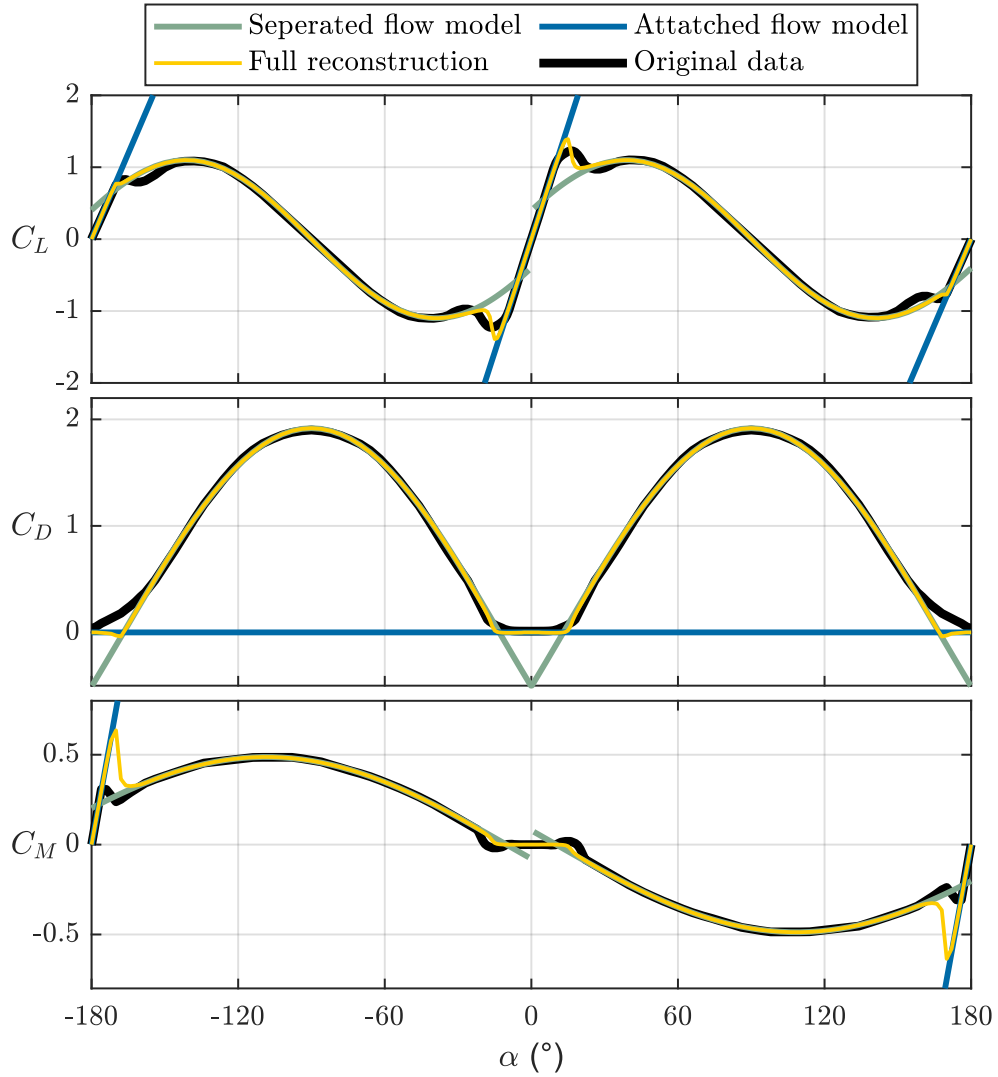


Figure 2: Quasisteady aerodynamic coefficient data for the wing aerofoil (ST50W), as a function of angle-of-attack (α), reconstructed from the GK attached and separated flow models, compared to the original data.

surfaces to model in this way: the wing surfaces and the horizontal and vertical stabilisers; the latter additionally modified by the elevator and rudder deflections. The two aerofoils in the system, the ST50W and ST50H, are modelled using the wing and stabiliser datasets from Selig [62]. Starting with the wing data; curve fitting indicates that it is approximated well (Fig. 2) by the relations:

$$\begin{aligned}
 C_{i,L, \text{sep}}(\alpha_i) &= a_{i,L} \operatorname{sgn} \alpha_i \sin(b_{i,L} |\alpha_i + c_{i,L}| + d_{i,L}) + e_{i,L}, \\
 C_{i,D, \text{sep}}(\alpha_i) &= a_{i,D} \sin(b_{i,D} |\alpha_i| + c_{i,D}) + d_{i,D}, \\
 C_{i,M, \text{sep}}(\alpha_i) &= a_{i,M} \operatorname{sgn} \alpha_i \sin(b_{i,M} |\alpha_i + c_{i,M}| + d_{i,M}) + e_{i,M},
 \end{aligned} \tag{5}$$

for all α_i , with model parameters $a_{i,j}$, $b_{i,j}$, $c_{i,j}$, $d_{i,j}$ and $e_{i,j}$; and for the leading and trailing edge considered separately:

$$\begin{aligned} C_{i,L, \text{att}}(\alpha_{l,i}) &= C_{i,L\alpha,l}\alpha_{l,i}, & C_{i,L, \text{att}}(\alpha_{t,i}) &= C_{i,L\alpha,t}\alpha_{t,i}, \\ C_{i,M, \text{att}}(\alpha_{l,i}) &= 0, & C_{i,M, \text{att}}(\alpha_{t,i}) &= C_{i,M\alpha,t}\alpha_{t,i}, \\ C_{i,D, \text{att}}(\alpha_{l,i}) &= 0, & C_{i,D, \text{att}}(\alpha_{t,i}) &= 0, \end{aligned} \quad (6)$$

where $\text{sgn } \alpha_i$ is the sign (signum) function, and $\alpha_{l,i}$ and $\alpha_{t,i}$ are the leading and trailing edge angles of attack (representing a partition of the full domain, $|\alpha_i| < 180^\circ$, into $|\alpha_i| \leq 90^\circ$ and $||\alpha_i| - 180^\circ| \leq 90^\circ$, the latter of which is mapped back to $|\alpha_i| \leq 90^\circ$ again.) Three of the attached flow models – $C_{i,M, \text{att}}(\alpha_{l,i})$ and both $C_{i,D, \text{att}}(\alpha_{l,i})$ – are observably zero. Note that the separated flow functions are still symmetric (odd or even) about $\alpha_i = 0$, as is expected for the symmetric aerofoil. The effect of aileron deflection is not considered, as this control function can be achieved by incidence morphing.

The parameters for these expressions are identified via nonlinear least-squares regression applied to selections of obviously attached and separated flow. $p_{0,i}$ can then also be estimated by solving $p_i = p_{0,i}$ in Eq. 3 using the empirical source data. Figure 3 shows the results of this process, compared to the traditional arctangent expression for $p_{0,i}(\alpha_i)$, as per Wickenheiser and Garcia [56] and Reich et al. [53]:

$$p_{0,i}(\alpha_i) = \begin{cases} 1 & |\alpha_i| < 4^\circ \\ -0.0058 \tan^{-1}(|\alpha_i| + 16) & 4^\circ \leq |\alpha_i| \leq 32^\circ \\ 0 & |\alpha_i| > 32^\circ. \end{cases} \quad (7)$$

For the trailing edge, this expression is modified to account for earlier and faster separation:

$$p_{0,i}(\alpha_{t,i}) = \begin{cases} 1 & |\alpha_{t,i}| < 4^\circ \\ -0.0058 \tan^{-1}(1.6|\alpha_{t,i}| + 16) & 4^\circ \leq |\alpha_{t,i}| \leq 21^\circ \\ 0 & |\alpha_{t,i}| > 21^\circ. \end{cases} \quad (8)$$

These results indicate that the arctangent $p_{0,i}$ is a reasonably accurate approximation for the ST50W. The quasisteady coefficient data for the ST50W wing may then be reconstructed for comparison. Figure 2 shows this data alongside the GK reconstruction using the arctangent p_0 (Eq. 7-8). The result is overall very good: the separated and attached flow regimes are modelled well. The most notable discrepancies are around the trailing edge transition in the

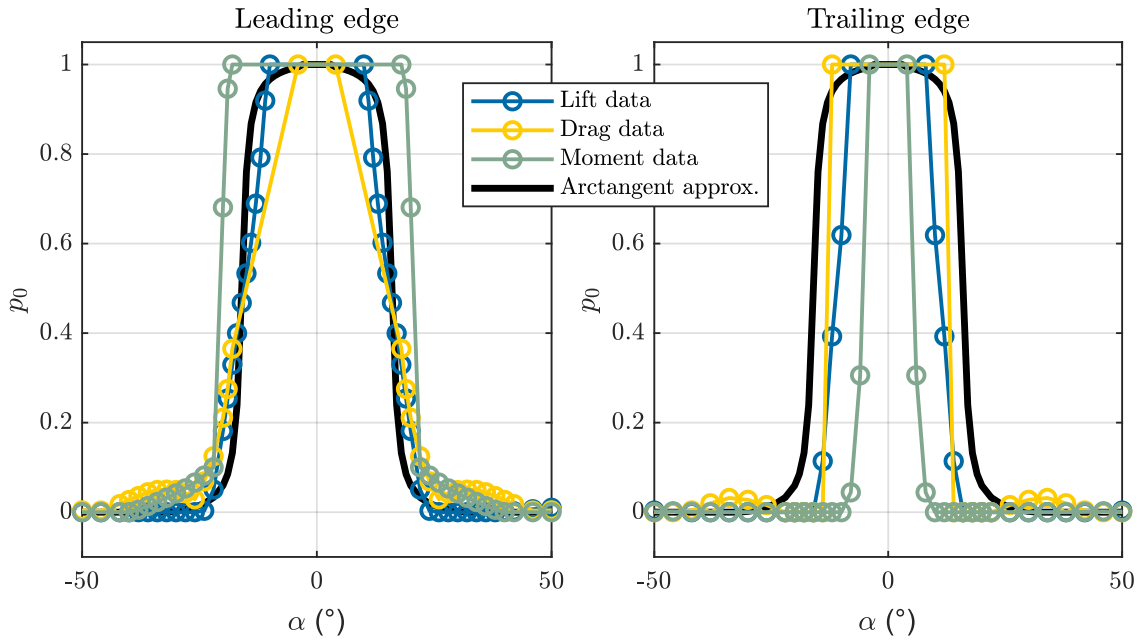


Figure 3: Filtered approximations to $p_{0,i}$ derived from wing aerofoil (ST50W) leading and trailing edge aerodynamic data, compared to the arctangent approximations.

drag and moment coefficients – as can be seen also in Fig. 3, the trailing edge drag and moment data appear to be requiring different $p_{0,i}$ functions. Such an approach however would destroy much of the remaining physical realism of the GK model – already only loosely connected to Goman and Khrabrov’s separation-point formulation [60,61] – and the potential increase in modelling accuracy is not large.

3.3. Stabiliser dynamic parameter identification

The aerodynamic data for our stabilizer aerofoil [62], presents the additional difficulty of a dependence on the stabiliser control surface deflection. To begin, quasistatic behaviour for the control-surface motion is assumed (*i.e.*, that the control-surface motion itself induces no flow). Although the dataset from Selig [62] contains aerodynamic coefficient data at seven different elevator deflections (-50° , -30° , -15° , 0° , 15° , 30° , 50°); only four of these are unique (*e.g.*, $\beta_e \in [-50, 0]^\circ$ or $\beta_e \in [0, 50]^\circ$). This is due to the symmetric aerofoil profile: downwards aerofoil motion at downwards control surface deflection is equivalent to upwards motion at upwards deflection. Selecting the unique set $\beta_e \in [-50, 0]^\circ$; for each control surface deflection data entry therein the attached and separated flow relations are identified according to a slightly modified model definition:

$$\begin{aligned}
C_{i,L, \text{sep}}(\alpha_i) &= a_{i,L} \operatorname{sgn}(\alpha_i + c_{i,L}) \sin(b_{i,L}|\alpha_i + c_{i,L}| + d_{i,L}) + e_{i,L}, \\
C_{i,D, \text{sep}}(\alpha_i) &= \begin{cases} a_{i,D} \cos(b_{i,D}|\alpha_i + c_{i,D}| + d_{i,D}) + e_{i,D}, & \beta_e = 0 \\ a_{i,D} \sin(b_{i,D}\alpha_i + c_{i,D}) + d_{i,D} & \text{o.w.}, \end{cases} \quad (9) \\
C_{i,M, \text{sep}}(\alpha_i) &= a_{i,M} \operatorname{sgn}(\alpha_i + c_{i,M}) \sin(b_{i,M}|\alpha_i + c_{i,M}| + d_{i,M}) + e_{i,M}.
\end{aligned}$$

with attached-flow models exactly as per Eq. 6. The key difference is the sinusoid drag model at nonzero β_e : the simpler model allows for an increased robustness in identification; the complexity of the coefficient data does not permit an easy identification of more complex models.

The identification is fully automated except for a manual indication of the location of areas of attached and separated flow for identification. The separated flow models are then smoothed with a Laplacian smoother to ease the interpolation across β_e . In the Supplementary material, the four unique identified models in each aerodynamic coefficient are presented. The final quasisteady functions required are the mixing parameter functions $p_{0,i}$. Figure 4 shows the estimates for these functions obtained by solving Eq. 3 for $p = p_0$ in the vicinity of the transition region. Estimates are available for C_L at the leading and trailing edge, and C_M at the trailing edge – areas where the attached flow model is nonzero. Estimates are given with respect to the reference angles-of-attack, $\alpha_{l,i,\text{ref}}$ and $\alpha_{t,i,\text{ref}}$: these values are the centre-points of the attached flow regions, specified manually, and nonzero for nonzero β_e .

A notable feature of these results is their asymmetry, with long tails at negative α (for $\beta_e < 0$). The assertion that this is a physical effect, and not a result of inaccuracy in the attached/separated flow models, may be supported by the empirical lift coefficient histories. At positive α values (for $\beta_e < 0$), large stall peaks are observed; whereas at negative α there is a flat plateau. Phenomenologically, this is thought to arise from flow reattachment effects when both the control surface and the aerofoil are inclined, *e.g.*, upwards ($\beta_e < 0$, $\alpha > 0$), leading to a state in which the control surface itself is effectively at low angle-of-attack. Conversely, for $\beta_e < 0$, $\alpha < 0$, more rapid flow separation is expected. The arctangent sigmoid of Reich [53] is not capable of capturing these asymmetric effects, and suffers from the further difficulty that the model parameters are not easily interpretable. To model both symmetric and asymmetric effects better, we propose a new GK sigmoid function, based on the logistic function. Its symmetric form, for the leading edge, is:

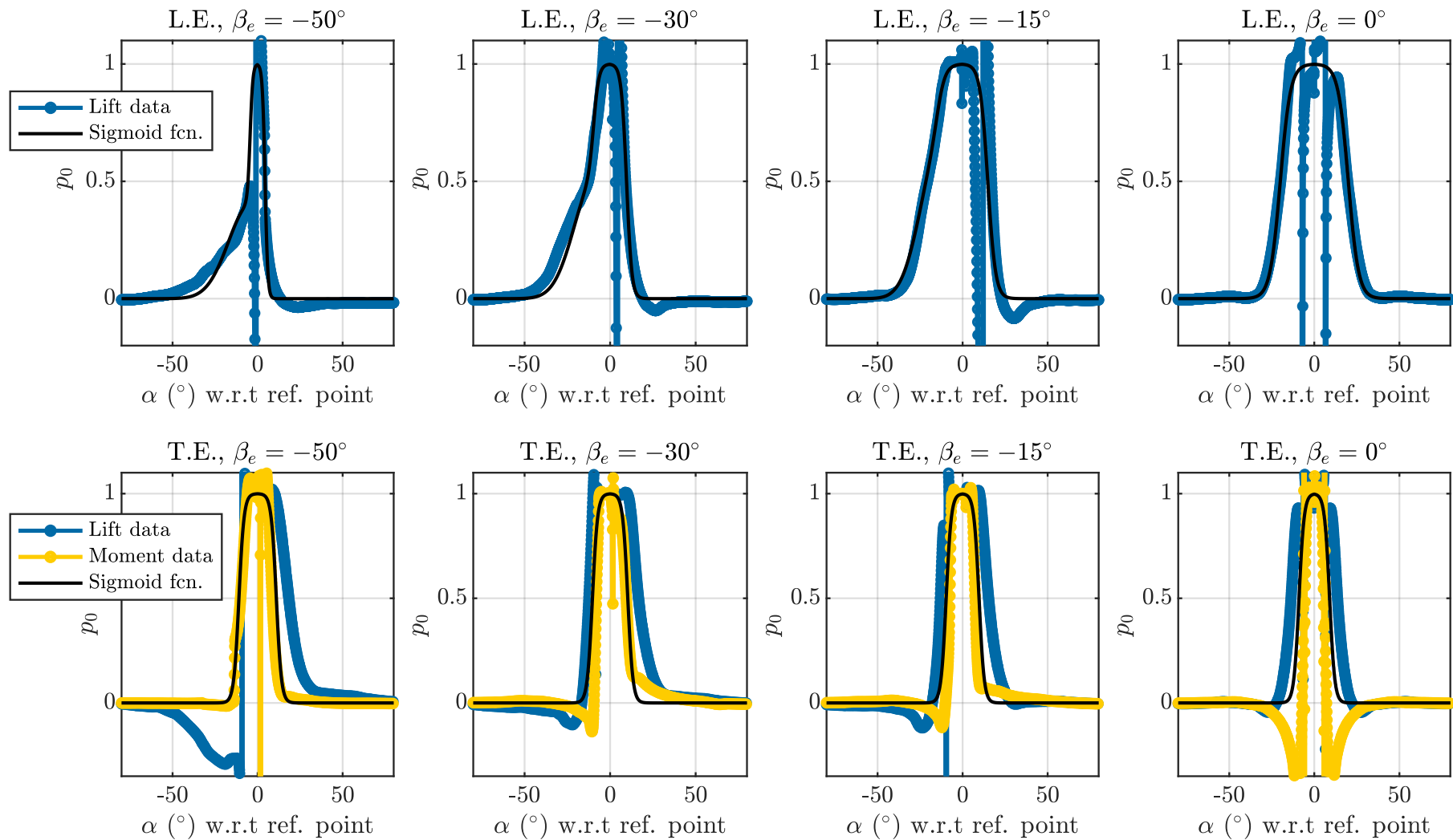


Figure 4: Unfiltered approximations to $p_{0,i}$ derived from stabiliser aerofoil (ST50H) leading edge (L.E.) and trailing edge (T.E.) aerodynamic data, against the associated logistic sigmoid fit.

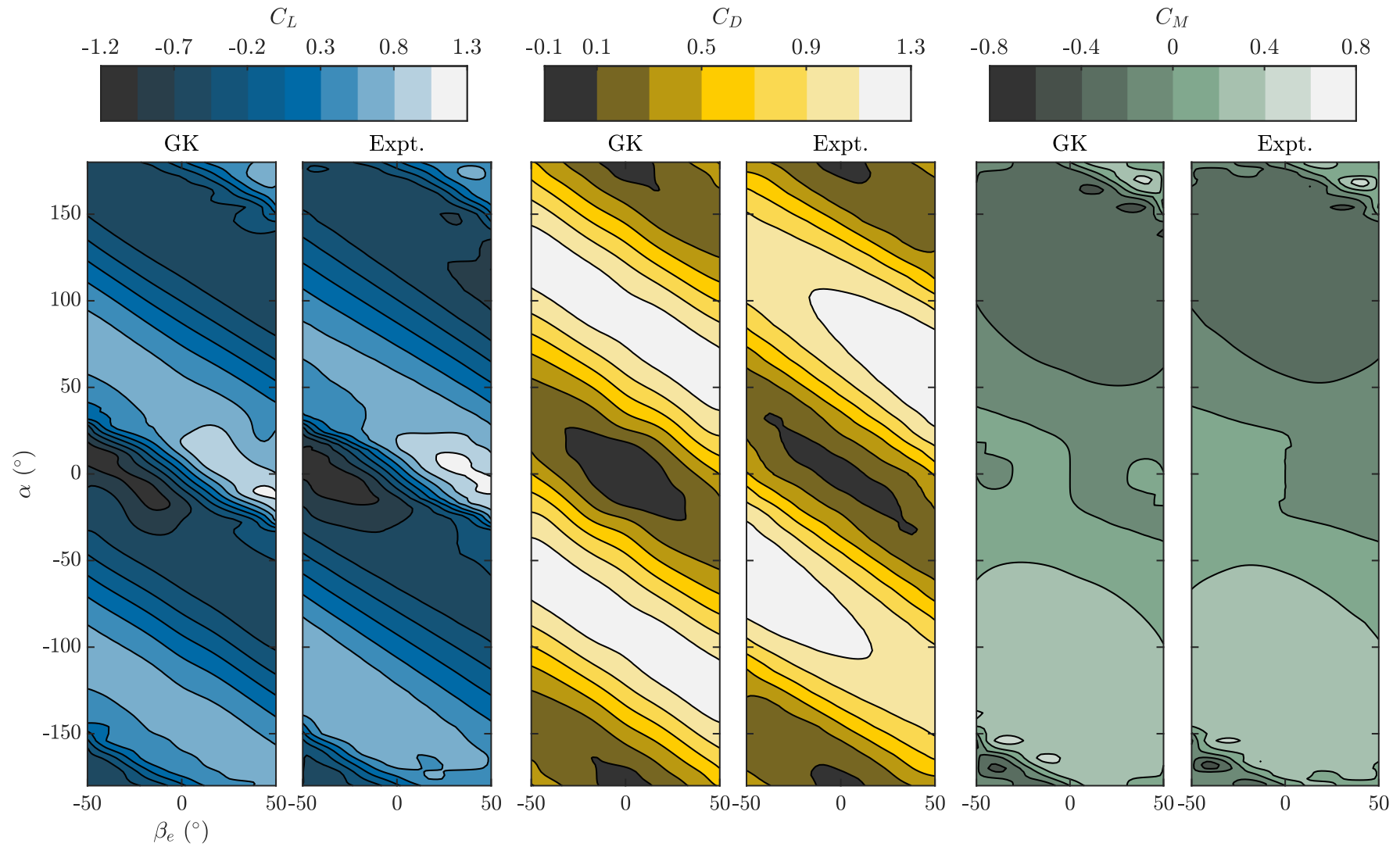


Figure 5: Quasisteady aerodynamic coefficient data for the stabiliser aerofoil (ST50H), as a function of both angle-of-attack (α) and control surface deflection (β_e), reconstructed from the GK attached and separated flow models, and compared to the original data.

$$p_{0,l,i,\text{sym}}(\alpha_{l,i}) = S\left(\frac{1}{m_{l,i}}(|\alpha_{l,i} - \alpha_{l,i,\text{ref}}| - \psi_{l,i})\right), \quad S(x) = \frac{1}{1 + \exp(x)}, \quad (10)$$

where $S(x)$ is the logistic function, $\alpha_{l,i,\text{ref}}$ is the centre point of the attached flow region (specified manually, and nonzero for nonzero β_e), and $(m_{l,i}, \psi_{l,i})$ are model parameters. The shift parameter $\psi_{l,i}$ is the α -value (w.r.t $\alpha_{l,i,\text{ref}}$) of the inflection or 50% point; that is $p_{0,l,i,\text{sym}}(\psi_{l,i} + \alpha_{l,i,\text{ref}}) = 0.5$. The width parameter $m_{l,i}$ governs the gradient at this point. The interpretable nature of these parameters is an aid to identification.

To account for the asymmetric nature of the empirical profiles, a one-sided Gaussian function is added to the symmetric sigmoid, to yield the completed $p_{0,l,i}$:

$$p_{0,l,i}(\alpha_{l,i}) = (1 - p_{0,i,\text{sym}}(\alpha_{l,i})) G(\alpha_{l,i}) + p_{0,i,\text{sym}}(\alpha_{l,i}), \quad (11)$$

$$G(\alpha_{l,i}) = M_{l,i} \exp\left(-\left(\frac{\alpha_{l,i} - \alpha_{l,i,\text{ref}} + \psi_{l,i}}{w_{l,i}}\right)^2\right) [\alpha_{l,i} - \alpha_{l,i,\text{ref}} < 0]_{\text{IV}},$$

where $w_{l,i}$ and $M_{l,i}$ are model parameters, $\psi_{l,i}$ is the parameter identified in Eq. 10, and $[\cdot]_{\text{IV}}$ is the Iverson bracket [65], such that $[s]_{\text{IV}} = 1$ if s is true, and $[s]_{\text{IV}} = 0$ if s is false. The nature of this addition ensures that the resulting profile is smooth (C^∞) over the halfspaces $\alpha_{l,i} > \alpha_{l,i,\text{ref}}$ and $\alpha_{l,i} < \alpha_{l,i,\text{ref}}$. The parameter $w_{l,i}$ governs the width of the Gaussian function, and the parameter $M_{l,i}$ its height.

In the case of the trailing edge, the discrepancy between the empirical p_0 estimates computed from C_L and C_M makes an asymmetric $p_{0,t,i}$ too difficult to identify. For this reason, the simple symmetric form is used:

$$p_{0,t,i,\text{sym}}(\alpha_{t,i}) = S\left(\frac{1}{m_{t,i}}(|\alpha_{t,i} - \alpha_{t,i,\text{ref}}| - \psi_{t,i})\right), \quad S(x) = \frac{1}{1 + \exp(x)}, \quad (12)$$

with model parameters $(m_{t,i}, \psi_{t,i})$ distinct from $(m_{l,i}, \psi_{l,i})$. For the four dataset points considered, leading- and trailing-edge p_0 parameters are estimated for $\beta_e = -50^\circ$ and $\beta_e = 0^\circ$; and then models at the internal surface-deflection points are generated by linearly interpolating model parameters. Table 2 shows the identified model parameters, including the associated interpolation index ($k \in [0, 1]$ for $\beta_e \in [-50, 0]^\circ$), and Fig. 4 the identified p_0 functions. The parameter interpolation is linear and two-point ($k \in \{0, 1\}$), with the exception of $M_{l,i}$, which

shows a rising trend with k but must necessarily be zero at $k = 1$ to preserve symmetry. For this reason, a non-monotonic piecewise-linear profile with the additional data-point $M_{l,i}(k = 0.75) = 0.6$ is used. These parameter variations are modelled at minimal complexity to maintain a reasonable level of model robustness and simplicity, consistent with the phenomenological nature of the model.

The resulting identified models can be extended to $\beta_e > 0$ by symmetry – pitch-up motion at positive deflection corresponding to pitch-down motion at negative deflection. The estimated quasisteady coefficient profiles can then be reconstructed using the relevant sigmoid $p_{0,i}$ expressions and the separated- and attached-flow models. Figure 5 shows the GK reconstruction of the ST50H quasisteady aerodynamic coefficients as a function of elevator deflection and α_i , compared with the original results of Selig [62]. The comparison is in contour format: at intermediate control surface deflections, the model functions (not their generative parameters) are interpolated. As can be seen, a generally good agreement is observed, despite some variation in the laminar-turbulent transition zones. The primary limitations of the identification are the discrepancy in identified separation point between the lift and moment coefficient data.

Table 2: Fitted model parameters for the logistic p_0 functions

Parameter	$\beta_e = -50^\circ$	$\beta_e = -30^\circ$	$\beta_e = -15^\circ$	$\beta_e = 0^\circ$
k	0	0.4	0.7	1
$\alpha_{l,i,\text{ref}}$	30.5°	19°	8°	0°
$\alpha_{t,i,\text{ref}}$	-148°	-162°	-172°	-180°
$m_{l,i}$	0.8	lin. interp.		3
$\psi_{l,i}$	4.4	lin. interp.		20
$M_{l,i}$	0.4	lin. interp. via 0.6 at $0.75k$		0
$w_{l,i}$	18	lin. interp.		14
$m_{t,i}$	1.5	constant		1.5
$\psi_{t,i}$	11	lin. interp.		9

3.4. Dynamic parameter identification

The GK model formulation for all lifting surfaces is nearly complete: the only unidentified parameters remaining are the delays $\tau_{1,i}$ and $\tau_{2,i}$. Transient aerodynamic data is required for their identification. In the current literature, experimental data is available for a variety of oscillating aerofoils, but not for the case study aerofoils (ST50W/H). The choice of these aerofoils was motivated both by their use in existing highly-maneuvrable UAVs, and

by the availability of aerodynamic data for all angles of attack and with control surface deflections. No aerofoils were found for which an existing complete dataset of transient and quasisteady aerodynamic data was available. Existing GK model identifications are also available for a few aerofoils, but the variation in identified delay parameters across similar or even identical aerofoils indicates that the GK-delays are strongly dependent on the GK-decomposed quasisteady model. Table 3 presents a range of delay parameters identified in the literature for three different aerofoils.

Table 3: GK delay parameters reported in the literature

Aerofoil	τ_1 (c/U)	τ_2 (c/U)	Source	Reynolds No.
NACA0009	2.5	2.0	An et al. [66]	4.9×10^4
	2.28	3.41	Reich et al. [53]	not stated
	2.6	2.8	Williams et al. [60]	5×10^4
	3.6	4.3	Williams et al. [63]	5.7×10^4
NACA0015	0.52	4.5	Goman [61]	c. 2×10^5
	2.14	13.56	Fan [67]	not stated
NACA0018	0.25	3.6	Williams et al. [60]	2.5×10^5
	1.57	1.52	Greenblatt et al. [68]	3×10^5
	1.73	4.83	Niel [69]	1.9×10^5

The variation across the reported values – with minimal change in Reynolds number – is large: for the NACA0009 factor of 2 variation (in τ_2) is observed across the reported values; for the NACA0012 a factor of 4 (in τ_1); and for the NACA0018 a factor of 7 (in τ_1). These results indicate that a precise identification of the delay parameters is sensitive to the dataset – potential factors include wind-tunnel/wall effects, surface roughness, and CFD modelling inaccuracies. This is consistent with the observation that the identification of the delay parameters is dependent on the aerofoil behaviour in the laminar-turbulent transition, and the projection to the hypothetical attached flow model at angles-of-attack below quasisteady stall: both of these factors are strongly dependent on modelling / dataset specifics.

A CFD process for modelling the ST50W aerofoil is described in [49]. From it we estimate $\tau_1 = \tau_2 = 2.3c/U$. This is broadly consistent with the NACA0009 estimates given in Table 3. Two upper bounds on this estimate, in terms of motion transience, are defined. The maximum permissible reduced frequency is $\kappa = b\Omega/U = 0.5$, where b is the local section

semichord, and Ω is the frequency (in rad/s) of aerofoil motion. The maximum permissible reduced pitch rate is $r = b\dot{\alpha}/U = 0.13$, where $\dot{\alpha}$ is the local section pitch rate. We note that there are several open questions with regard to how to integrate GK dynamic stall models into a flight simulation context [49]: most significantly, exactly how the delay parameters should be taken to scale with local station airspeed (U), given that this airspeed will vary. We take these delay parameters to scale with U , according to the dimensional relation $\tau_1 = \tau_2 = 2.3c/U$, but further research is required to establish this relationship with confidence.

3.5. Combined model framework

The GK model is now complete, defining the aerodynamic force function $Q_A(\mathbf{z}, \mathbf{v})$ in the system dynamics (Eq. 2). The combination of GK and multibody-dynamic models for our biomimetic UAV lead to the complete system:

$$\begin{aligned} & \begin{bmatrix} \mathbf{B}_1(\mathbf{z}, \mathbf{v}) & \\ & \mathbf{T}_1(\mathbf{z}, \mathbf{v}) \end{bmatrix} \begin{bmatrix} \dot{\mathbf{z}} \\ \dot{\mathbf{p}} \end{bmatrix} \\ & = \begin{bmatrix} \mathbf{f}(\mathbf{z}, \mathbf{p}, \mathbf{v}) \\ \mathbf{p}_0(\boldsymbol{\alpha}(\mathbf{z}, \mathbf{v}) - \mathbf{T}_2(\mathbf{z}, \mathbf{v})\dot{\boldsymbol{\alpha}}(\mathbf{z}, \mathbf{v})) \end{bmatrix} + \begin{bmatrix} -\mathbf{B}_0(\mathbf{z}, \mathbf{v}) & \\ & \mathbf{I} \end{bmatrix} \begin{bmatrix} \mathbf{z} \\ \mathbf{p} \end{bmatrix}, \end{aligned} \quad (13)$$

where the terms in \mathbf{p} and $\dot{\mathbf{p}}$ represent the flow attachment dynamics (Eq. 4) over all lifting surfaces, and the terms in \mathbf{z} and $\dot{\mathbf{z}}$ represent the UAV multibody dynamics (Eq. 2). The addition of the flow attachment dynamics significantly increases the size of the system under integration. According to a mesh independence study, five aerodynamic stations along each lifting surface is sufficient to keep errors in overall lifting surface lift, drag and moment below 1% for the manoeuvres we will study. This leads to an aerodynamic system $(\mathbf{p}, \dot{\mathbf{p}})$ with 25 degrees of freedom, in addition to the 12 degrees of freedom of the first-order multibody dynamics model $(\mathbf{z}, \dot{\mathbf{z}})$. We will now apply this flight dynamic models to the understanding of supermanoeuvrability in biological and biomimetic systems.

4. RaNPAS: the Pugachev cobra

4.1. Motivation and manoeuvre design

The Pugachev cobra is a simple pitch-only supermanoeuvre which involves tilting the UAV backwards from level flight to beyond 90° pitch angle, and then forwards to level flight again, while maintaining approximately constant altitude [18]. As such it is a form of RaNPAS capability as per Gal-Or [15]; and although no such RaNPAS capability is observed in

biological flight, the cobra manoeuvre is widespread among supermanoeuvrable aircraft. At the simplest level, recreating a cobra manoeuvre in our biomimetic morphing-wing UAV requires the identification of three control configurations: **(i)** an initial trim configuration, **(ii)** a configuration to generate the moment required to pitch the UAV upwards, to the partially inverted position; and **(iii)** a configuration to pitch the UAV forwards from the partially inverted position, and back to the trim configuration. We note that the trim configuration **(i)** is computable via existing methods [48,49]. This trim configuration may indeed be a candidate for configuration **(iii)**, however, to find other more general candidates, we utilise a more general approach, as follows.

Firstly: as this manoeuvre is constrained to the x - z plane, the control space for manoeuvre design is constrained also by symmetry about this plane. Potential active degrees of freedom are thus the symmetric dihedral Γ ($\theta_{wl} = \theta_{wr} = \Gamma$), the symmetric sweep Λ ($\psi_{wl} = -\pi/2 - \Lambda$, $\psi_{wr} = \pi/2 + \Lambda$), and the symmetric incidence α ($\phi_{wl} = \phi_{wr} = \alpha$) the elevator deflection β_e , and the propulsive force F_{prop} . Some of these degrees of freedom are constrained: we enforce control limits on the elevator deflection ($|\beta_e| < 0.87$ rad) and wing sweep ($0.4 \leq |\psi_w| \leq \pi - 0.4$ rad, *i.e.*, $|\Lambda| < 1.171$ rad). Secondly, for initial manoeuvre design purposes we utilise a quasisteady aerodynamic model, based on the initial quasisteady data [62]. The purpose of this initial model simplification is to permit a characterisation of the UAV's nonlinear longitudinal and lateral static stability profiles. We will optimise these profiles to generate candidate control configurations for the manoeuvre, which we will then test and verify under both quasisteady and transient (GK) aerodynamic models.

As regards the generation of these candidate configurations: over the control space, we then define objective functions related to the intended behaviour of the configuration. Multiple objective functions are available. Consider first the pitch-up configuration, **(ii)**, above. The UAV point pitch accelerations at low to medium-high angles of attack, $\ddot{\theta}(\theta_i)$ provide simple and physically-relevant metrics to maximise. More complex functions include the pitch acceleration integral ($\int \ddot{\theta}(\theta) d\theta$), and the location of the roots of the UAV nonlinear longitudinal and lateral static stability profile: $\theta : \ddot{\theta}(\theta) = 0$. We refer to this latter root as a *quasi-trim* state: this state is momentarily at a pitch equilibrium ($\ddot{\theta} = 0$), and indeed, momentarily at an orientation equilibrium, by the symmetry constraint. However, it is not at an

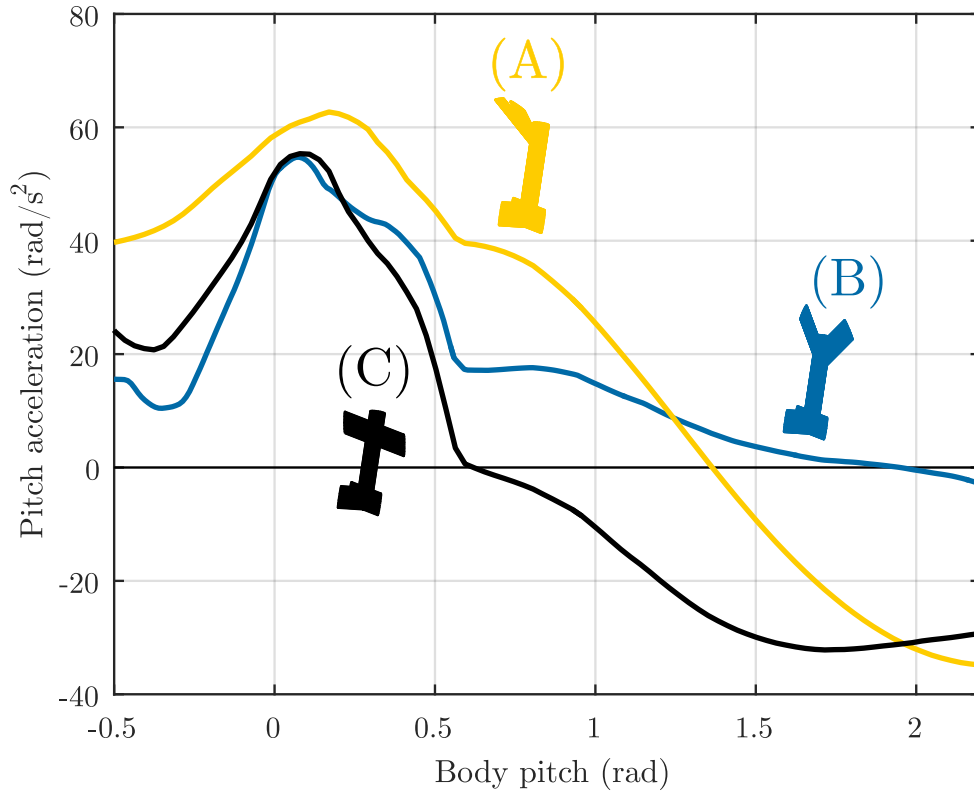


Figure 6: Static longitudinal stability profile of several candidate pitch-up configurations: (A) with all morphing DOF enabled; (B) with only sweep (Λ) and incidence (α) DOF enabled; (C) with only the incidence DOF enabled. The key feature of these profiles is the degree to which a positive (upwards) pitch acceleration is maintained at high angles of attack: the longer a positive acceleration is maintained, the greater the maximum attainable angle-of-attack during a RaNPAS manoeuvre.

equilibrium in translational degrees of freedom (airspeed, or altitude), and so is eventually likely to deviate from an orientation equilibrium, as changes in airspeed and altitude / altitude rate eventually propagate to changes in pitch dynamics. The process may be analogised with fast-slow behaviour in dynamical systems [70]. Quasi-trim states will be of significant relevance to our characterisation of pitch-axis supermanoeuvrability.

As an initial objective function, we use the point pitch acceleration at a pitch value of 0.8 rad (46°). Figure 6 shows several control configurations generated by pitch-up configuration optimization. Results A-C indicate pitch stability plots for optimal configurations with (A) all degrees of freedom active, (B) sweep and incidence active and (C) only incidence active. The associated wing configuration is rendered alongside. Note that $U = 30$ m/s and $F_{\text{prop}} = 10$ N as a reference [48,49], *cf.* Table 1. In the case of (A), however, note that significant additional pitch-up moment can be generated by the offset between the propulsive

force axis and the centre of mass due to the upwards wing dihedral. Parameter values for these configurations are given in Table 4; values in bold type are located on their respective constraint limits, and indicate the effect of these constraints on the configuration performance. For example, in all states the elevator is at its control limit, and it is self-evident that increased elevator control effectiveness will result in greater pitch control effectiveness. At very high angles of attack (> 1 rad), however, the elevator ceases to have a significant effect on the system pitch dynamics, and morphing controls must take over. In the fully-actuated system (A), the sweep degree of freedom is at its control limit, indicating that improvements in sweep control effectiveness (*e.g.*, via larger wing chord) would result in greater pitch control effectiveness. However, the Λ - α system, case (B), is not at any control limits, indicating that more complex effects are also at play, for example the balance between the lift- and drag-generated pitch-up moment, and the optimisation trade-off that increased sweep represents for these two moments.

Table 4: Parameters for optimal pitch-up configurations. Values in bold type are located on their respective constraint limits.

Parameter	(A) All DOF	(B) Λ - α	(C) α
Γ (rad)	0.730	0	0
Λ (rad)	1.171	0.699	0
α (rad)	0.247	0.181	0.171
β_e (rad)	-0.870	-0.870	-0.870

The wing parameters associated with a high pitch-up rate are a positive dihedral, forward wing sweep and mild upwards inclination. Upwards inclination increases the wing lift, but too much reduces the drag-induced pitch-back moment at high angles of attack. Positive dihedral, in combination with forward sweep, induces a pitch-back drag moment even at low angles of attack. The forward sweep is particularly relevant, as this shifts the aerodynamic centre further forward and thus increases its pitching moment about the centre of mass (which is less strongly affected by the sweep motion). The result is that the UAV's stable pitch quasi-trim configuration (the pitch equilibrium $\dot{\theta} = 0$) is shifted to a very to a high angle of attack (in result (B), even to the partially-inverted position) thus providing a strong attraction towards that flight state. While result (B) has a quasi-trim configuration at the highest angle of attack, the strength of its attraction is significantly weaker than that of result (A), as indicated by the pitch acceleration gradient at the quasi-trim configuration. Result (A) is thus likely to allow the

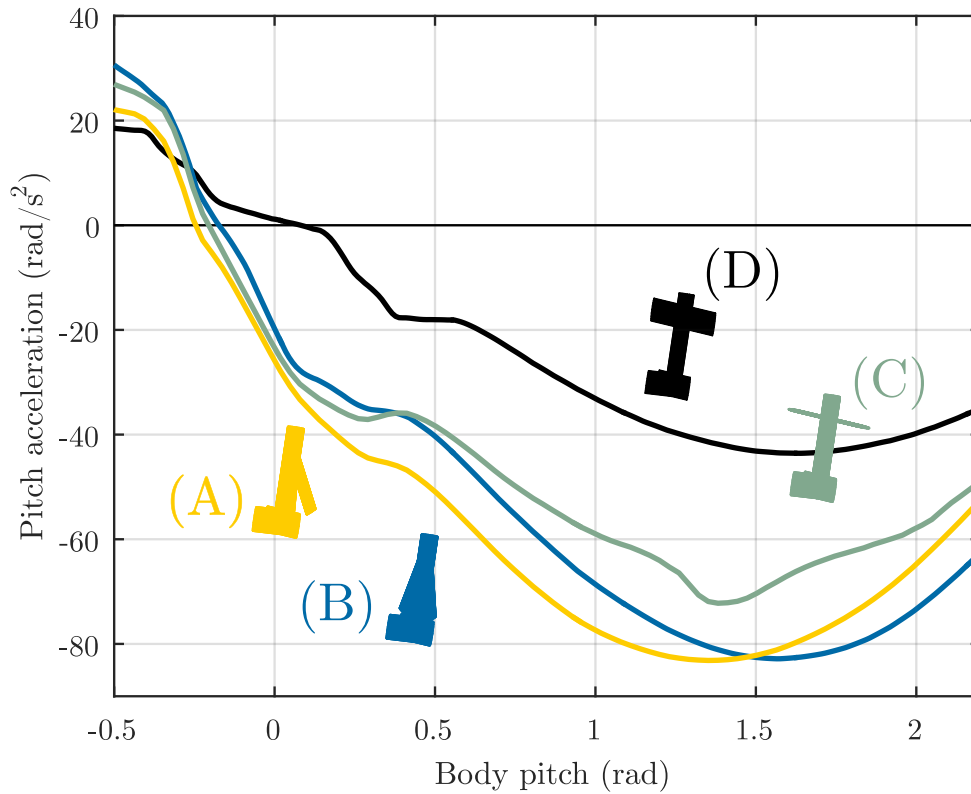


Figure 7: Static longitudinal stability profile of several candidate pitch-down configurations: (A) with all morphing DOF enabled; (B) with only sweep (Λ) and incidence (α) DOF enabled; (C) with only the incidence DOF enabled; (D) the initial trim configuration. The key feature of these profiles is the strength of the negative (downwards) pitch acceleration at high angles of attack ($> 90^\circ$): the greater the negative pitch acceleration, the more likely that the UAV can recover from a high-angle-of-attack states.

cobra manoeuvre to be carried out more rapidly, and without interference from the untrimmed variables. In any case, the transient overshoot to the c. $\theta = 1.4$ rad trim configuration will take the UAV to higher angles. Note that the use of forward sweep in does have the disadvantage of decreasing the aeroelastic divergence speed of the wings [71], limiting the flight envelope of these forward-swept configurations.

For the pitch-down configuration similar objective functions are available; though the relevant pitch angles for pitch acceleration minimization are higher (>1 rad). Figure 7 shows configurations to minimise the point pitch acceleration at 1.4 rad pitch, and Table 5 shows their parameter values. Results A-C are the optimal configurations for (A) all degrees of freedom active, (B) sweep and incidence active and (C) only incidence active. Result (D) is an example trim configuration, at $\Gamma = 0$, $\psi_{tgt} = 0$, and $\theta_{tgt} = 0.08$ rad – a non-optimal but obvious default candidate, with minimal control deflection. Similar aerodynamic effects to those in Figure 6

are observed. Backward sweep moves the aerodynamic centre rearwards, and the presence of anhedral allows the maximum wing surface area to be inclined into the flow, for maximum restoring drag moment. In these cases, the wing incidence is kept flat to make use of this restoring drag moment; however, when only incidence motion is available, inclining the lifting surface into the local free-stream to reduce its drag is the better option. The tail then provides all the available restoring moment. This configuration has the additional benefit of generating significant lift at high angles of attack; thus reducing the burden on the propulsion during the manoeuvre. The trim configuration itself, as a result of the airframe stability, generates moderate pitch-up acceleration; but this acceleration can be doubled in the presence of wing morphing.

Table 5: Parameters for optimal pitch-down configurations. Values in bold type are located on their respective constraint limits.

Parameter	(A) All DOF	(B) Λ - α	(C) α	(D) Trim
Γ (rad)	-0.255	0	0	0
Λ (rad)	-1.171	-1.171	0	0
α (rad)	0.168	0.0493	-1.654	0.014
β_e (rad)	0.262	0.262	0.262	0.003

4.2. Flight simulation of a 3DOF-morphing cobra manoeuvre

With candidate pitch-up and pitch-down configurations identified, we may simulate several differing forms of cobra manoeuvre. We start with the simplest to define. The UAV begins at an initial trim state; then changed to the 3DOF (all-DOF) pitch-up configuration, as per Fig. 6 and Table 4; and then returns to the original trim state. The only free variables left are the timings of these configurations: these timings can be defined by closed-loop control, automatic tuning, or, as we use here, simple manual tuning. Figure 8 shows the flight simulation results for a simple cobra manoeuvre of this form, including the UAV flight path, its control and orientation history, and its acceleration history compared with the quasistatic states (Fig. 6-7). This simulation is performed under the full GK aerodynamic model. The initial and final near-trim state is the trim state at pitch 0.08 rad and airspeed 30 m/s; with the system initialised at pitch 0.08 rad and airspeed 40 m/s. The time-scales of the morphing motion are 500 ms in the near-trim state, 100 ms transition, 50 ms in the trim-up state and then an immediate return to the near-trim state. This discontinuous control path is then smoothed strongly via a Laplacian smoother, leading to the final control commands of Figure 8. The manoeuvre is successful: the UAV reaches a nose-up state ($\theta = 1.56$ rad) within half a second of the control onset, losing

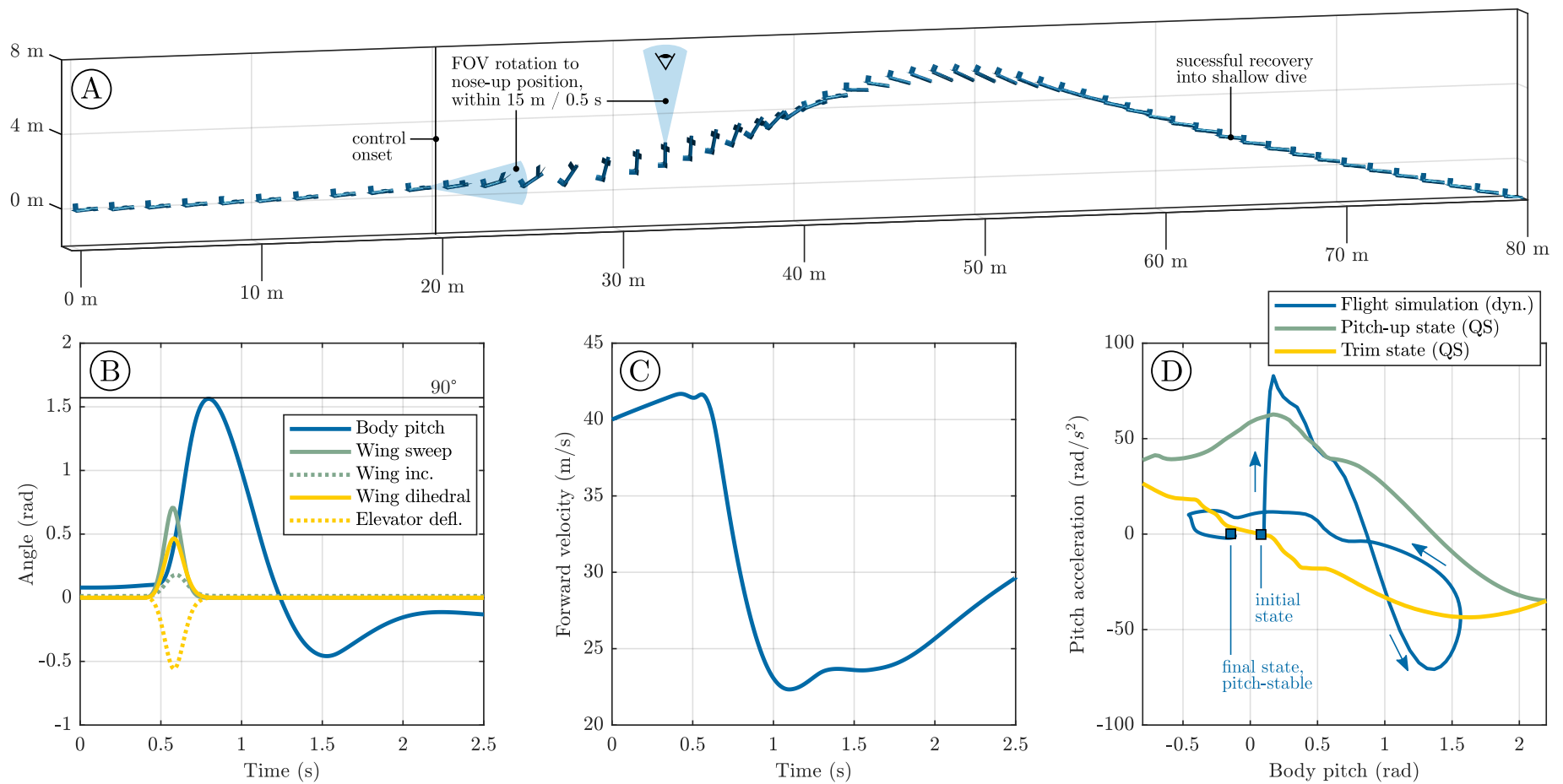


Figure 8: Flight simulation results for a simple 3DOF-morphing cobra manoeuvre at $T/W = 0.25$, under a quasisteady aerodynamic model. **(A)** flight path with UAV rendered every 50 ms ($0 \leq t \leq 2.5$ s); **(B)** control and orientation history; **(C)** forward velocity history; and **(D)** acceleration history compared with the quasistatic acceleration profiles are shown. The UAV configuration sequence is: near-trim \rightarrow optimal pitchup \rightarrow near-trim.

19 m/s of airspeed in the process (a reduction of 46%). The UAV then regains airspeed as it transitions into a shallow dive, though not without notable pitch-down overshoot – the UAV reaching a pitch-down peak of -0.46 rad (-26°). The manoeuvre is roughly altitude neutral, as altitude gain due to the vertical thrust component at peak pitch offsets the altitude loss of the dive recovery. Finally, it is interesting to compare the dynamic pitch acceleration history of the UAV to the quasistatic nonlinear longitudinal stability profiles of the control configurations (Fig. 8D). During the early pitch-up manoeuvre, the quasistatic pitch-up configuration profile represents the dynamic profile relatively well, but, by the point of the peak pitch angle, the dynamic profiles differ significantly – a difference attributable to dynamic pitching effects and airspeed loss. Despite the difference, the manoeuvre is performed successfully, indicating that heuristics based on longitudinal stability profiles can be a successful strategy for designing supermanoeuvres in biomimetic UAVs.

4.3. Flight simulation of a 2DOF-morphing cobra manoeuvre

The 3DOF-morphing cobra manoeuvre studied in Section 4.2 is high-performance, but this level of morphing complexity may not be feasible in all systems. We are interested in reducing the control complexity required to successfully perform a cobra manoeuvre in this system. Considering the candidate configurations studied in Section 4.1 (Fig. 6-7), we observe that the sweep-incidence (Λ - α) morphing combination can achieve similar levels of pitch-up and pitch-down strength to the full 3DOF combination. We observe, in particular, that it is the addition of sweep morphing that shifts the quasi-trim point of the pitch-up configuration (Fig. 6) to a point at greater than 90° pitch. Physically, this corresponds to forward motion of the UAV aerodynamic centre, generating strong pitch-up moment. In manoeuvre design terms, this bodes well for the use of sweep-incidence morphing for the generating the required initial pitch-up moment.

However, simply chaining together the sweep-incidence candidate states given in Section 4.1 does not lead to a successful manoeuvre: the pitch-up moment is insufficient to bring the UAV to beyond 90° pitch. Instead, we add another manoeuvre component. Previous analysis of this case study morphing-wing UAV [48,49] revealed the existence of a space of morphed UAV trim states across pitch and yaw: a space of states, at different fuselage orientations, that each could represent a steady level flight state. To reduce the pitch-up moment requirement in the main stage of the manoeuvre, we use these morphed trim states to

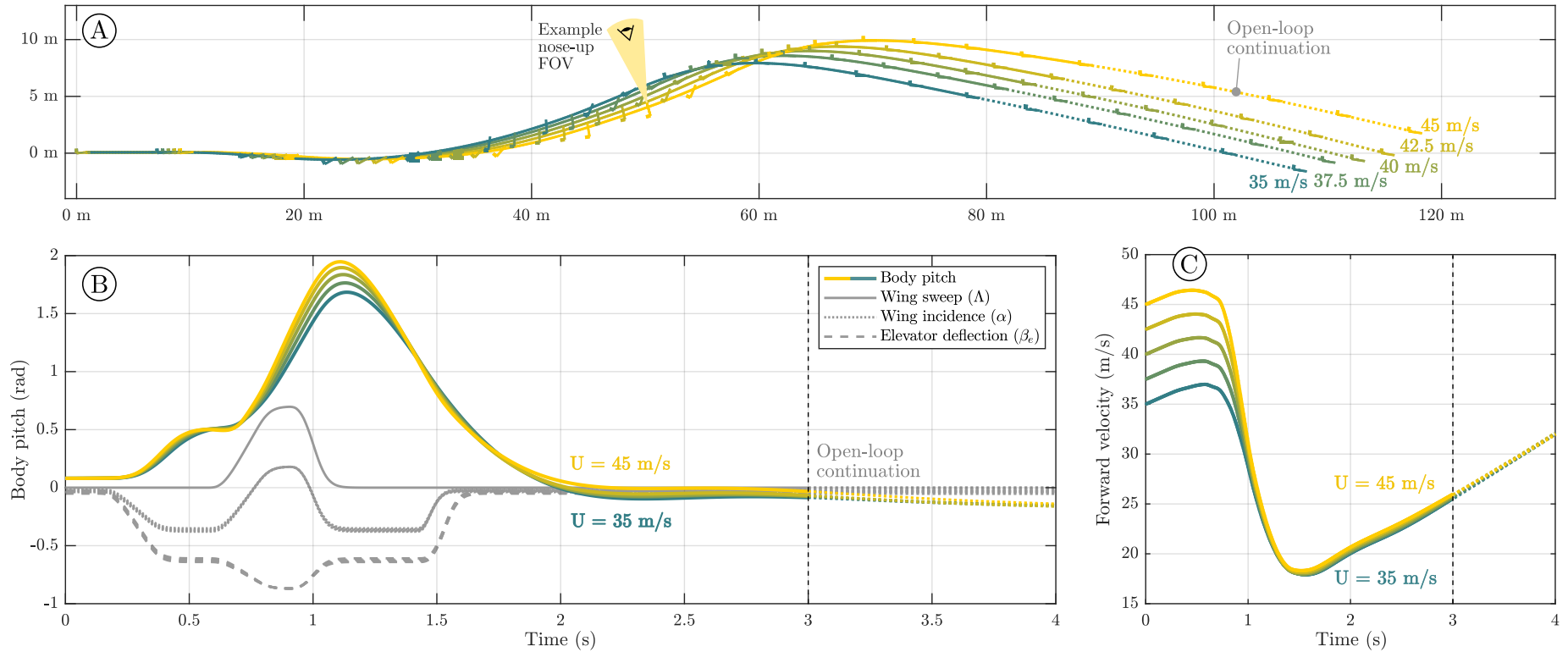


Figure 9: Flight simulation results for a 2DOF-morphing cobra manoeuvre at $T/W = 0.25$, with varying initial airspeed, and using the full GK aerodynamic model. (A) flight path with UAV rendered every 200 ms ($0 \leq t \leq 4$ s); (B) control and orientation history; (C) forward velocity history. The UAV configuration sequence is: near-trim at $\alpha = 0$ rad \rightarrow trim at $\alpha = 0.4$ rad \rightarrow optimal pitchup \rightarrow trim at $\alpha = 0.4$ rad \rightarrow near-trim at $\alpha = 0$ rad. Beyond $t = 3$ s, the open-loop response of the UAV (a shallow dive) is simulated, as an illustration of the post-manoevre recovery process. In reality, beyond $t = 3$ s is the region in which conventional manual or automatic closed-loop flight control would be expected to be reactivated, to pursue whatever post-manoevre objective is relevant.

bring the UAV up to its maximum trim state pitch of 0.5 rad (29°) (Fig. 9), over a short duration. From this point we use the candidate pitch-up and pitch-down configurations of Section 4.1 to generate a cobra manoeuvre. This manoeuvre is successful: Fig. 9 shows the resulting set of cobra manoeuvres that can be achieved at differing initial airspeeds. In general, these manoeuvres show better performance than the manoeuvre in Fig. 8: they have a greater peak pitch angle (up to 1.95 rad), minimal pitch-down overshoot during the recovery phase (down to only -0.096 rad), and smaller altitude loss. The manoeuvre is, however, less rapid, with the peak pitch point occurring within two seconds of the control onset – a consequence of the initial trim-state alteration. This manoeuvre highlights the significance of trim space analysis, as per [48,49], to the study of biomimetic supermanoeuvrability: trim space manoeuvres, or quasistatic NPAS (QNPAS), can form an important component in rapid NPAS (RaNPAS).

5. Biomimetic manoeuvrability: the ballistic transition

5.1. Motivation and manoeuvre design

RaNPAS manoeuvres such as the Pugachev Cobra have no direct parallels in biological supermanoeuvrability. This may indeed be connection with the close association with weapons and equipment based on field-of-view (cannon, missiles, *etc.*) rather than on direct contact (beaks, talons, *etc.*). In biological creatures, the absence of field-of-view weapons would be expected to render true RaNPAS manoeuvres of minimal utility – and indeed, such manoeuvres have either not evolved or are not commonly observed. Nevertheless, some forms biological manoeuvre do show correspondences with more general forms of NPAS capability; though their motivation is not primarily to effect orientation changes. One such manoeuvre is the ballistic transition, observed in a variety of gliding mammals [12,13,36]. The ballistic transition manoeuvre is similar to a cobra manoeuvre, but with no pitch-down configuration: the objective is to decrease the airspeed of the UAV in preparation for an impact landing on a vertical surface. As such, manoeuvre design for a ballistic transition manoeuvre in our biomimetic UAV can proceed along fundamentally the same lines as Section 4.1. We utilise a simple modification of the cobra controls: we generate a pitch-up moment via a 2DOF (Λ - α) morphing pitch-up configuration (Table 4, Fig. 6), but instead of transitioning subsequently to a pitch-down configuration, the UAV transitions to a neutral configuration which maintains a high pitch angle at decreasing airspeed until the point of impact. A useful example of a conveniently-located near-neutral configuration is very same pitch-up state but with zero

incidence and elevator deflection (*i.e.*, only forward sweep). In a manoeuvre of maximum simplicity, this state may be maintained until impact landing – as we will now simulate.

5.2. Manoeuvre simulation

Figure 10 shows a simulation of a ballistic transition manoeuvre in the biomimetic UAV, under the GK aerodynamic model, and utilising the 2DOF (sweep-incidence, Λ - α) sequence of control configurations studied in Fig. 6. The objective is a low-velocity impact landing on the vertical surface of a building, 45 m away, starting at forward velocity of 60 m/s. The effect of a varying constant thrust value ($0.2 < T/W < 1$) is shown. For all the simulated thrust values, the ballistic transition manoeuvre is successful, for a single set of control timings: the UAV lands in an almost exact vertical position, with both the horizontal and vertical velocity < 12 m/s. Even in the worst case, $T/W = 0.2$, the system kinetic energy is reduced by 94% at the point of impact, with near-zero altitude change. The primary effect of T/W is to increase the altitude gain through the manoeuvre, reducing the system kinetic energy via transfer to gravitational potential. Maximal levels of kinetic energy dissipation (up to 97.5%) are thus associated with maximal available thrust (at least, up to $T/W = 1$). However, the effect of T/W on the aerodynamic energy dissipation is only secondary, as evidenced by the total energy trends: optimal total energy dissipation occurs at $T/W = 0.6$, but the variation is not large. The use of altitude gain for kinetic energy is useful but **i**) may or may not be permissible in the context of the impact landing, and **ii**) may be achievable through finer morphing control at lower T/W . We note also that the use of forward sweep, and the corresponding reduction in wing aeroelastic divergence speed, is likely to limit the initial airspeed of the manoeuvre: a more versatile manoeuvre sequence is to use incidence morphing (and, if available, dihedral) for initial airspeed reduction before a sweep morphing phase. Aeroelastic tailoring is also an option to increase the divergence speed [72,73].

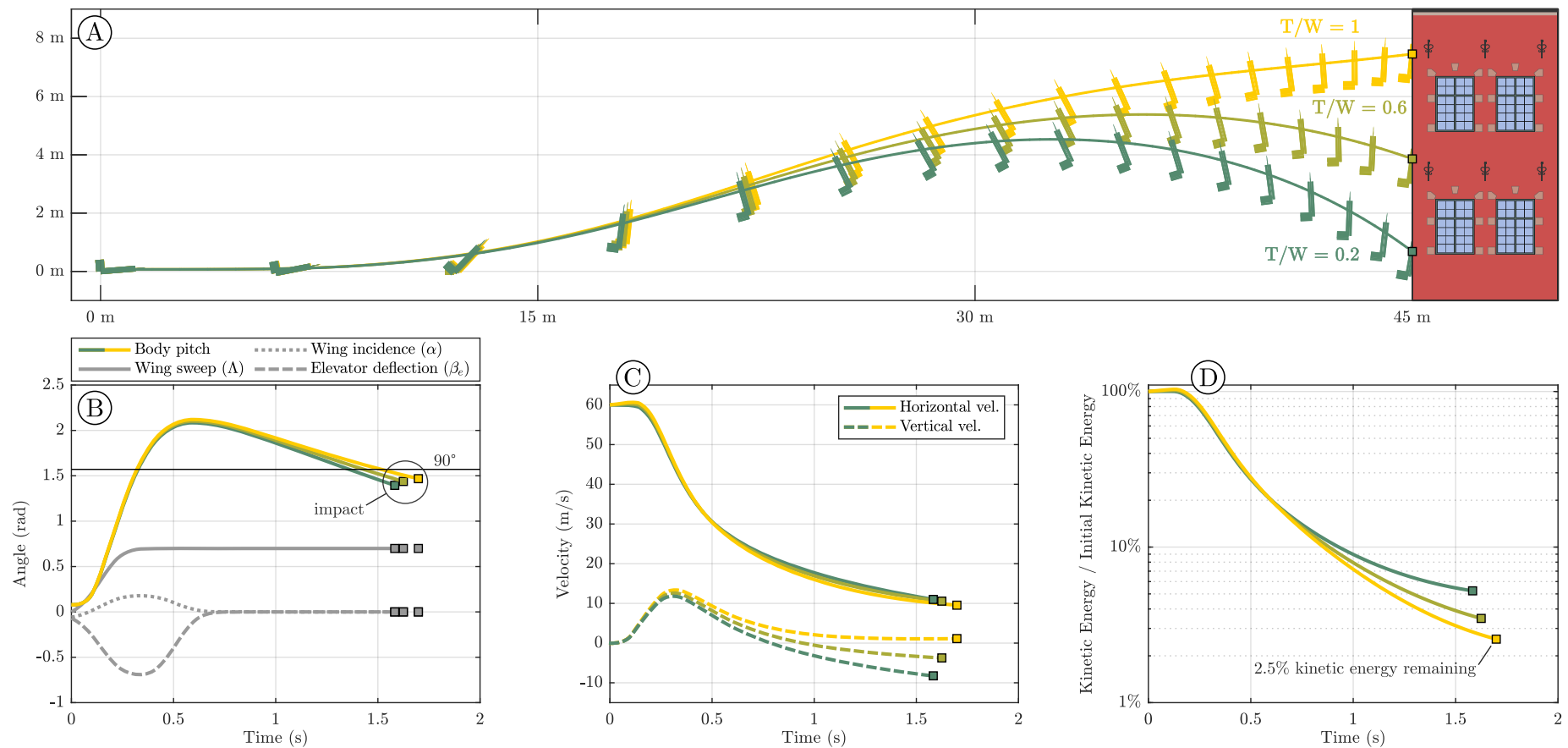


Figure 10: Flight simulation results for a 2DOF-morphing ballistic transition manoeuvre with initial velocity 60 m/s, under varying initial thrust (T/W). The UAV configuration sequence is: trim \rightarrow pitchup \rightarrow stabilisation state. **(A)** UAV flight paths, overlaid on an illustrative scenario involving landing on a building. **(B)** Body pitch angle histories and control histories, indicating the varying point of impact landing. **(C)** Horizontal and vertical velocity histories. **(D)** Relative kinetic energy history, indicating that in the best case ($T/W = 1$), the impact landing occurs with only 2.5% of the UAV's initial kinetic energy.

6. Effects of aerodynamic model fidelity

6.1. Model fidelity effects in a cobra manoeuvre context

The simulations in Sections 4.2-4.3 were performed with the modified GK dynamic stall model devised in Section 3: a model which captures hysteretic dynamic stall effects on all of the UAV's lifting surfaces. Two relevant questions can be formulated regarding the role of this model in the manoeuvres studied in Sections 4-5. Firstly: how significant are hysteretic dynamic stall effects in these manoeuvres? And secondly: how do these manoeuvres fit into the ranges of model validity outlined in Section 3.4? Considering the simple 3DOF cobra manoeuvre of Section 4.2, Fig. 11 illustrates flight simulation results (pitch angle and flight path) for three different aerodynamic models: **i)** the quasisteady model based on original source data; **ii)** the GK-reconstructed quasisteady model, with $p = p_0$ (Sections 3.2-3.3); **iii)** the transient GK model with full dynamic stall effects. Figure 9 also illustrates the wing- and stabiliser-tip lift coefficient histories for the four simulations, and provides an assessment of the full transient GK simulation in terms of reduced frequency and reduced pitch rate, with the thresholds for GK and quasisteady model validity noted.

As can be seen, the cobra manoeuvre in this biomimetic UAV is remarkably resilient to dynamic stall effects: while these effects do cause significant changes in the manoeuvre lift coefficient peaks, these changes do not fundamentally alter the nature of the manoeuvre. Several explanations for this resilience are available. **i)** The GK model does not directly model pre-stall transient effects (*e.g.*, Wagner / Theodorsen effects) and in this situation these may be a more significant factor than dynamic stall effects; which require a stall transition. **ii)** The cobra manoeuvre may show intrinsic high levels of stability in simulation, arising from the planar nature of the manoeuvre – eliminating the possibility of roll drift. This may explain why the large but short-timescale lift peaks arising from delayed separation do not significantly perturb the manoeuvre. **iii)** In addition, the symmetric nature of the hysteresis loop (with delayed stall and delayed reattachment) may serve to self-cancel in a sufficiently stable system. The planar assumption obviously neglects more complex transient effects arising from asymmetric forebody separation [74–77]; if uncontrolled, these could initiate a GK-based destabilisation. The uncertain nature of these effects implies that, in a real system, they may be more significant, and may require a control response.

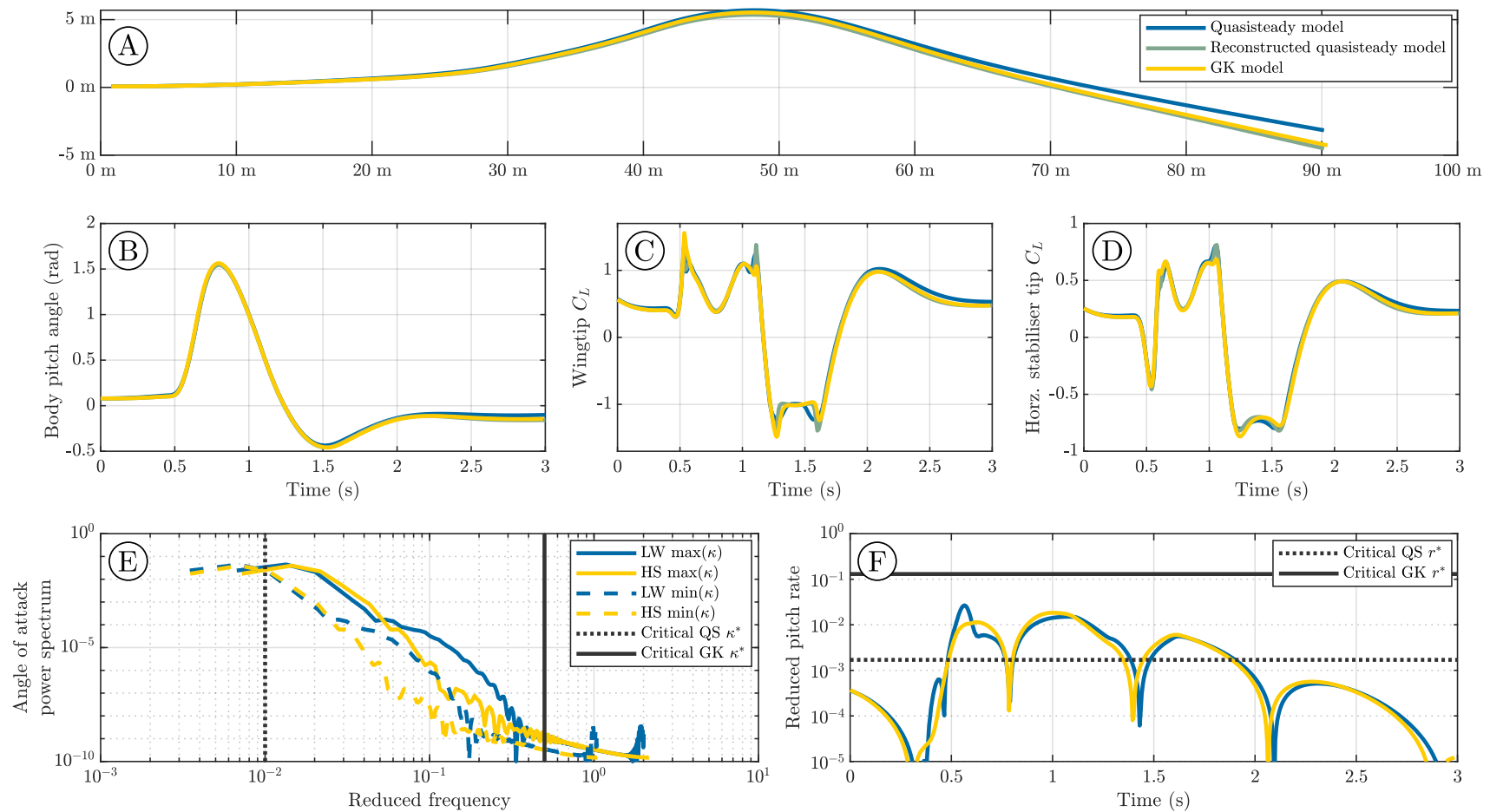


Figure 11: Validation flight simulation results for a simple 3DOF-morphing cobra manoeuvre at $T/W = 0.25$: simulations with the quasisteady (QS) aerodynamic model; with the GK-reconstructed quasisteady aerodynamic model; and with the full GK model (lift, drag, moment). **(A)** Flight path; **(B)** Orientation history; **(C)** Wingtip lift coefficient; **(D)** Horizontal stabiliser tip lift coefficient; **(E)** Angle of attack power spectrum, indicating the approximate limits of QS and GK model validity. **(F)** Reduced pitch rate profile, indicating the approximate limits of QS and GK model validity. As can be seen, the manoeuvre lies within the limits of GK model validity; and, despite lying partly outside the limits of QS model validity, is well-approximated in simulation.

6.2. Model fidelity effects in a ballistic transition manoeuvre context

We can perform the same analysis on a ballistic transition manoeuvre, as per Section 5. Taking the highest-performance manoeuvre at $T/W = 1$, we perform the same three simulations: **i**) with the quasisteady aerodynamic model based on original source data; **ii**) with the GK-reconstructed quasisteady model, with $p = p_0$ (Sections 3.2-3.3); and **iii**) with the full transient GK model. Figure 12 shows the results of these simulations, including an assessment of the full transient GK simulation in terms of reduced frequency and reduced pitch rate, with the thresholds for GK and quasisteady model validity noted. The results are notably different to the cobra manoeuvre results of Section 6.1. The same relatively brief differences in lift coefficient peak (due to lift hysteresis) are present, but in the ballistic transition manoeuvre, they have a significant effect. Lift hysteresis effects alter the aerodynamic behaviour of both the wings and horizontal stabiliser during the pitch-up segment of the manoeuvre ($0 \leq t \leq 0.5$); an alteration which then propagates to significant changes in the UAV flight path, and its kinetic energy at the point of impact landing.

These changes are all the more interesting because the manoeuvre transience, as measured, for instance, by the reduced pitch rate, is not particularly large – only just straying into the region in which the quasisteady model is expected to be invalid ($r \geq 0.0017$). In practical terms, unlike the cobra manoeuvre studied in Section 6.1, this ballistic transition manoeuvre is not resilient to aerodynamic uncertainty (*vis-à-vis* lift hysteresis), perhaps due to the absence of any pitch-down manoeuvre segment which might serve as a self-cancellation mechanism. This highlights the importance of considering dynamic stall effects when designing and controlling ballistic transition manoeuvres in biomimetic and other UAVs. Note also that further out-of-plane effects, such as asymmetric forebody separation, may also be at work, and may require additional control response. Asymmetric forebody separation in biomimetic UAVs is an interesting topic for future research: existing studies, focusing on manned combat aircraft, typically consider delta wing geometries [74–77], rather than the forward-swept wing configuration used in this biomimetic UAV. The extent to which the results of these analyses apply in the forward-swept case is currently uncertain.

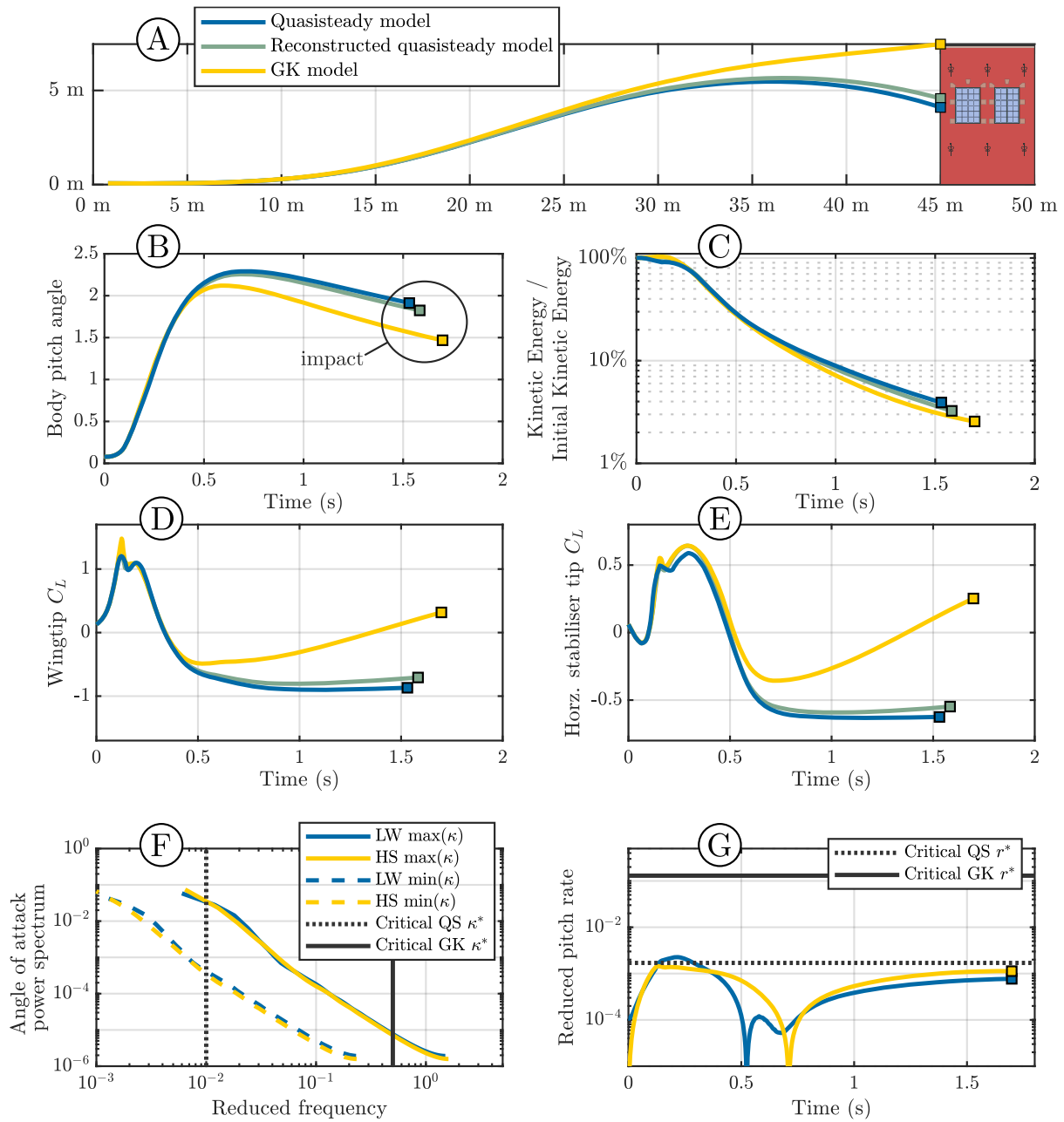


Figure 12: Validation flight simulation results for a ballistic transition manoeuvre at $T/W = 1$: simulations with the quasisteady (QS) aerodynamic model; with the GK-reconstructed quasisteady aerodynamic model; and with the full GK model (lift, drag, moment). (A) Flight path; (B) Orientation history; (C) Relative kinetic energy history; (D) Wingtip lift coefficient; (E) Horizontal stabiliser tip lift coefficient; (F) Angle of attack power spectrum, indicating the approximate limits of QS and GK model validity. (G) Reduced pitch rate profile, indicating the approximate limits of QS and GK model validity. As can be seen, the manoeuvre lies within the limits of GK model validity; and, despite lying partly outside the limits of QS model validity, is well-approximated in simulation.

Finally, note that in this ballistic transition manoeuvre, the reduced frequency (κ) is not a reliable metric of lifting surface aerodynamic transience: the UAV airspeed changes significantly, leading to significant uncertainty in the value of the appropriate airspeed (U) used in the reduced frequency calculation ($\kappa = b\Omega/U$). Figure 12 shows only coarse estimates based on maximum and minimum airspeed. As a result of the time-frequency uncertainty principle (the Gabor limit) [78], it is intrinsically impossible to locate spectral components of a signal (Ω) precisely in time (t , and therefore U), and it is thus intrinsically impossible to provide exact manoeuvre time-histories for reduced frequency κ . However, improvements over the current max-min approach may be available, via the use of short-time Fourier transforms [79,80].

7. Discussion and conclusion

In this work we have demonstrated, for the first time, that classical supermanoeuvrability is available in biomimetic UAVs. Pitch-axis RaNPAS, in the form of the cobra manoeuvre, is demonstrated in multiple variants and across multiple aerodynamic models. This supermanoeuvrability is achievable without thrust vectoring: it is instead achieved via biomimetic wing morphing. While there are several limitations regarding closed-loop control, and out-of-plane aerodynamic effects, this novel demonstration that classical supermanoeuvrability is possible via biomimetic wing morphing is a fundamental advance in our understanding of aerial manoeuvrability. It provides an impetus for the practical development of supermanoeuvrable biomimetic UAVs, as well as raising several further lines of research, and open questions. For instance: in what contexts is thrust-vectoring supermanoeuvrability preferable to morphing-wing supermanoeuvrability? Are there manoeuvres which are possible via one of these mechanisms, but not the other? We can already identify several contexts in which morphing-wing supermanoeuvrability might be preferable. Morphing-wing supermanoeuvrability does not rely on thrust to effect orientation changes, and thus requires relatively low thrust-weight values – indeed, these manoeuvres may be possible at a glide state. Morphing-wing supermanoeuvrability is also directly relevant to the control of flapping-wing aircraft, and even, to understanding the manoeuvrability of biological flying creatures. The guidance method demonstrated in this paper, based on control of the UAV longitudinal stability profile, may be applicable to the design of supermanoeuvres in flapping-wing UAVs.

In this work, we also explored the connection between classical supermanoeuvrability and biological flight manoeuvrability in more depth: we demonstrated how a high-performance biological flight manoeuvre – the ballistic transition manoeuvre – is available in the same biomimetic UAV, and can be generated via the same manoeuvre design strategy. Indeed, in this biomimetic UAV, the ballistic transition manoeuvre is found to be closely related to the classical cobra manoeuvre: both can be achieved by cycling through the same morphing configurations. This not only highlights the commonality between classical supermanoeuvrability and biological flight manoeuvrability, but paves the way for the applications of biological manoeuvrability in UAVs: for instance, UAVs capable of rapid landing on vertical or inverted surfaces. In this work, we focused on pitch-axis manoeuvrability, but further study of biological flight manoeuvrability along other flight axes – including biological stall turns [4–7], and zero-air-speed rolling manoeuvres [11] – could lead to further novel forms of UAV manoeuvrability. The intersection between classical supermanoeuvrability, biological flight manoeuvrability, and morphing-wing aircraft is a cross-disciplinary topic with the potential to significantly advance our understanding of aerial manoeuvrability, and to lead to new designs of military and industrial UAV.

Declaration of competing interest

The authors declare that they have no known competing financial interests or personal relationships that could have appeared to influence the work reported in this paper.

Acknowledgements

This work was supported by the Cambridge Commonwealth Trust.

References

- [1] A.C. Carruthers, A.L.R. Thomas, S.M. Walker, G.K. Taylor, Mechanics and aerodynamics of perching manoeuvres in a large bird of prey, *Aeronaut. J.* 114 (2010) 673–680. <https://doi.org/10.1017/S0001924000004152>.
- [2] C. Greatwood, A. Waldock, T. Richardson, Perched landing manoeuvres with a variable sweep wing UAV, *Aerosp. Sci. Technol.* 71 (2017) 510–520. <https://doi.org/10.1016/j.ast.2017.09.034>.
- [3] M. Feroskhan, T.H. Go, Dynamics of sideslip perching maneuver under dynamic stall influence, *Aerosp. Sci. Technol.* 50 (2016) 220–233. <https://doi.org/10.1016/j.ast.2016.01.005>.
- [4] D.R. Warrick, Bird Maneuvering Flight: Blurred Bodies, Clear Heads, *Integr. Comp. Biol.* 42 (2002) 141–148. <https://doi.org/10.1093/icb/42.1.141>.

- [5] J.S. Altenbach, Locomotor morphology of the vampire bat, *Desmodus rotundus*, *Spec. Publ. Am. Soc. Mammal.* (1979) 1–135. <https://doi.org/10.5962/bhl.title.39538>.
- [6] J.A. Gillies, A.L.R. Thomas, G.K. Taylor, Soaring and manoeuvring flight of a steppe eagle *Aquila nipalensis*, *J. Avian Biol.* 42 (2011) 377–386. <https://doi.org/10.1111/j.1600-048X.2011.05105.x>.
- [7] X. Tian, J. Iriarte-Diaz, K. Middleton, R. Galvao, E. Israeli, A. Roemer, A. Sullivan, A. Song, S. Swartz, K. Breuer, Direct measurements of the kinematics and dynamics of bat flight, *Bioinspir. Biomim.* 1 (2006) S10–S18. <https://doi.org/10.1088/1748-3182/1/4/S02>.
- [8] M.A. Ogilvie, D.I.M. Wallace, Field identification of grey geese, *Br. Birds.* 68 (1975) 57–67.
- [9] A.E. Pete, D. Kress, M.A. Dimitrov, D. Lentink, The role of passive avian head stabilization in flapping flight, *J. R. Soc. Interface.* 12 (2015) 20150508. <https://doi.org/10.1098/rsif.2015.0508>.
- [10] S. Marchant, P.J. Higgins, *Handbook of Australian, New Zealand & Antarctic Birds. Volume 1, Ratites to ducks; Part B, Australian pelican to ducks*, Oxford University Press, Melbourne, Australia, 1990.
- [11] D. Warrick, K.P. Dial, Kinematic, aerodynamic and anatomical mechanisms in the slow, maneuvering flight of pigeons, *J. Exp. Biol.* 201 (1998) 655–672. <https://doi.org/10.1242/jeb.201.5.655>.
- [12] M. Ando, S. Shiraishi, Gliding flight in the Japanese giant flying squirrel *Petaurista leucogenys*, *J. Mammal. Soc. Jpn.* 18 (1993) 19–32. <https://doi.org/10.11238/jmammsocjapan.18.19>
- [13] B.J. Stafford, R.W. Thorington Jr., T. Kawamichi, Gliding Behavior of Japanese Giant Flying Squirrels (*Petaurista Leucogenys*), *J. Mammal.* 83 (2002) 553–562. [https://doi.org/10.1644/1545-1542\(2002\)083<0553:GBOJGF>2.0.CO;2](https://doi.org/10.1644/1545-1542(2002)083<0553:GBOJGF>2.0.CO;2).
- [14] W.B. Herbst, Future fighter technologies, *J. Aircr.* 17 (1980) 561–566. <https://doi.org/10.2514/3.44674>.
- [15] B. Gal-Or, *Vectored Propulsion, Supermaneuverability and Robot Aircraft.*, Springer, New York, NY, 2013.
- [16] D.A. Joyce, *Flying beyond the stall: the X-31 and the advent of supermaneuverability*, NASA, Washington, DC, 2014.
- [17] G.E. Erickson, High Angle-of-Attack Aerodynamics, *Annu. Rev. Fluid Mech.* 27 (1995) 45–88. <https://doi.org/10.1146/annurev.fl.27.010195.000401>.
- [18] L.E. Ericsson, Cobra maneuver unsteady aerodynamic considerations, *J. Aircr.* 32 (1995) 214–216. <https://doi.org/10.2514/3.46706>.
- [19] K. Huenecke, *Modern Combat Aircraft Design*, Airlife, Shrewsbury, UK, 1994.
- [20] P.G. Hamel, ed., *In-Flight Simulators and Fly-by-Wire/Light Demonstrators*, Springer, Cham, Switzerland, 2017. <https://doi.org/10.1007/978-3-319-53997-3>.
- [21] D. Mackenzie, A Flapping of Wings, *Science.* 335 (2012) 1430–1433. <https://doi.org/10.1126/science.335.6075.1430>.

- [22] J.W. Gerdes, S.K. Gupta, S.A. Wilkerson, A Review of Bird-Inspired Flapping Wing Miniature Air Vehicle Designs, *J. Mech. Robot.* 4 (2012) 021003. <https://doi.org/10.1115/1.4005525>.
- [23] T.A. Ward, M. Rezaadad, C.J. Fearday, R. Viyapuri, A Review of Biomimetic Air Vehicle Research: 1984–2014, *Int. J. Micro Air Veh.* 7 (2015) 375–394. <https://doi.org/10.1260/1756-8293.7.3.375>.
- [24] Z. Hui, Y. Zhang, G. Chen, Aerodynamic performance investigation on a morphing unmanned aerial vehicle with bio-inspired discrete wing structures, *Aerosp. Sci. Technol.* 95 (2019) 105419. <https://doi.org/10.1016/j.ast.2019.105419>.
- [25] D. Xu, Z. Hui, Y. Liu, G. Chen, Morphing control of a new bionic morphing UAV with deep reinforcement learning, *Aerosp. Sci. Technol.* 92 (2019) 232–243. <https://doi.org/10.1016/j.ast.2019.05.058>.
- [26] S. Qin, Z. Weng, Z. Li, Y. Xiang, H. Liu, On the controlled evolution for wingtip vortices of a flapping wing model at bird scale, *Aerosp. Sci. Technol.* 110 (2021) 106460. <https://doi.org/10.1016/j.ast.2020.106460>.
- [27] M. Keennon, K. Klingebiel, H. Won, Development of the Nano Hummingbird: A Tailless Flapping Wing Micro Air Vehicle, in: 50th AIAA Aerosp. Sci. Meet. New Horiz. Forum Aerosp. Expo., AIAA, Nashville, TN, 2012. <https://doi.org/10.2514/6.2012-588>.
- [28] J. Zhang, F. Fei, Z. Tu, X. Deng, Design optimization and system integration of robotic hummingbird, in: 2017 IEEE Int. Conf. Robot. Autom. ICRA, IEEE, Singapore, 2017: pp. 5422–5428. <https://doi.org/10.1109/ICRA.2017.7989639>.
- [29] D. Bie, D. Li, J. Xiang, H. Li, Z. Kan, Y. Sun, Design, aerodynamic analysis and test flight of a bat-inspired tailless flapping wing unmanned aerial vehicle, *Aerosp. Sci. Technol.* 112 (2021) 106557. <https://doi.org/10.1016/j.ast.2021.106557>.
- [30] J. Colorado, A. Barrientos, C. Rossi, K.S. Breuer, Biomechanics of smart wings in a bat robot: morphing wings using SMA actuators, *Bioinspir. Biomim.* 7 (2012) 036006. <https://doi.org/10.1088/1748-3182/7/3/036006>.
- [31] S.J. Furst, G. Bunget, S. Seelecke, Design and fabrication of a bat-inspired flapping-flight platform using shape memory alloy muscles and joints, *Smart Mater. Struct.* 22 (2013) 014011. <https://doi.org/10.1088/0964-1726/22/1/014011>.
- [32] M.Y. Zakaria, H.E. Taha, M.R. Hajj, Design Optimization of Flapping Ornithopters: The Pterosaur Replica in Forward Flight, *J. Aircr.* (2015) 1–12. <https://doi.org/10.2514/1.C033154>.
- [33] J.M. Harris, K.S. Maloney, *Petauroides volans* (Diprotodontia: Pseudocheiridae), *Mamm. Species.* 42 (2010) 207–219. <https://doi.org/10.1644/866.1>.
- [34] P.G. Dolan, D.C. Carter, *Glaucomys volans*, *Mamm. Species.* (1977) 1. <https://doi.org/10.2307/3504026>.
- [35] K.L. Bishop, W. Brim-Deforest, Kinematics of turning maneuvers in the southern flying squirrel, *Glaucomys volans*, *J. Exp. Zool. Part Ecol. Genet. Physiol.* 309 (2008) 225–242. <https://doi.org/10.1002/jez.447>.
- [36] S.M. Jackson, Glide angle in the genus *Petaurus* and a review of gliding in mammals, *Mammal Rev.* 30 (2000) 9–30. <https://doi.org/10.1046/j.1365-2907.2000.00056.x>.

- [37] S.A. Kane, A.H. Fulton, L.J. Rosenthal, When hawks attack: animal-borne video studies of goshawk pursuit and prey-evasion strategies, *J. Exp. Biol.* 218 (2015) 212–222. <https://doi.org/10.1242/jeb.108597>.
- [38] H.D. Aldridge, Turning flight of bats, *J. Exp. Biol.* 128 (1987) 419–425. <https://doi.org/10.1242/jeb.128.1.419>.
- [39] D. Evangelista, S. Cam, T. Huynh, A. Kwong, H. Mehrabani, K. Tse, R. Dudley, Shifts in stability and control effectiveness during evolution of Paraves support aerial maneuvering hypotheses for flight origins, *PeerJ.* 2 (2014) e632. <https://doi.org/10.7717/peerj.632>.
- [40] M. Wang, L. Wang, T. Yue, H. Liu, Influence of unmanned combat aerial vehicle agility on short-range aerial combat effectiveness, *Aerosp. Sci. Technol.* 96 (2020) 105534. <https://doi.org/10.1016/j.ast.2019.105534>.
- [41] A.P. Pope, J.S. Ide, D. Micovic, H. Diaz, D. Rosenbluth, L. Ritholtz, J.C. Twedt, T.T. Walker, K. Alcedo, D. Javorsek, Hierarchical Reinforcement Learning for Air-to-Air Combat, in: 2021 Int. Conf. Unmanned Aircr. Syst. (ICUAS), IEEE, Athens, Greece, 2021: pp. 275–284. <https://doi.org/10.1109/ICUAS51884.2021.9476700>.
- [42] J. Yoo, D. Kim, D.H. Shim, Deep Reinforcement Learning based Autonomous Air-to-Air Combat using Target Trajectory Prediction, in: 2021 21st Int. Conf. Control Autom. Syst. (ICCAS), IEEE, Jeju, Republic of Korea, 2021: pp. 2172–2176. <https://doi.org/10.23919/ICCAS52745.2021.9649876>.
- [43] J. Flanagan, R. Strutzenberg, R. Myers, J. Rodrian, Development and Flight Testing of a Morphing Aircraft, the NextGen MFX-1, in: 48th AIAA/ASME/ASCE/AHS/ASC Struct. Struct. Dyn. Mat. Conf., AIAA, Honolulu, HI, 2007. <https://doi.org/10.2514/6.2007-1707>.
- [44] M.S. Selig, Real-Time Flight Simulation of Highly Maneuverable Unmanned Aerial Vehicles, *J. Aircr.* 51 (2014) 1705–1725. <https://doi.org/10.2514/1.C032370>.
- [45] J.B. Dunning, ed., CRC handbook of avian body masses, CRC Press, Boca Raton, FL, 2008.
- [46] G.V.T. Matthews, C.R.G. Campbell, Weights and measurements of Greylag Geese in Scotland, *Wildfowl.* 20 (1969) 86–93.
- [47] J.R. Speakman, D. Banks, The function of flight formations in Greylag Geese *Anser anser*; energy saving or orientation?, *Ibis.* 140 (2008) 280–287. <https://doi.org/10.1111/j.1474-919X.1998.tb04390.x>.
- [48] A. Pons, F. Cirak, Multiaxis nose-pointing-and-shooting in a biomimetic morphing-wing aircraft, *arXiv* (2021). <https://arxiv.org/abs/2201.03601>.
- [49] A. Pons, Supermanoeuvrability in a biomimetic morphing-wing aircraft, PhD Thesis, University of Cambridge, 2019.
- [50] J. Lankford, D. Mayo, I. Chopra, Computational investigation of insect-based flapping wings for micro air vehicle applications, *Int. J. Micro Air Veh.* 8 (2016) 64–78. <https://doi.org/10.1177/1756829316646640>.
- [51] V. Dwivedi, M. Damodaran, Computational Aeromechanics of a Maneuvering Unmanned Aerial Vehicle with Variable-Incidence Wings, *J. Aircr.* 52 (2015) 1914–1926. <https://doi.org/10.2514/1.C033102>.

- [52] M. Goman, A. Khrabrov, State-space representation of aerodynamic characteristics of an aircraft at high angles of attack, *J. Aircr.* 31 (1994) 1109–1115. <https://doi.org/10.2514/3.46618>.
- [53] G.W. Reich, F.E. Eastep, A. Altman, R. Albertani, Transient Poststall Aerodynamic Modeling for Extreme Maneuvers in Micro Air Vehicles, *J. Aircr.* 48 (2011) 403–411. <https://doi.org/10.2514/1.C000278>.
- [54] A. Wickenheiser, E. Garcia, Aerodynamic Modeling of Morphing Wings Using an Extended Lifting-Line Analysis, *J. Aircr.* 44 (2007) 10–16. <https://doi.org/10.2514/1.18323>.
- [55] B. Mi, H. Zhan, S. Lu, An extended unsteady aerodynamic model at high angles of attack, *Aerosp. Sci. Technol.* 77 (2018) 788–801. <https://doi.org/10.1016/j.ast.2018.03.035>.
- [56] A.M. Wickenheiser, E. Garcia, Optimization of Perching Maneuvers Through Vehicle Morphing, *J. Guid. Control Dyn.* 31 (2008) 815–823. <https://doi.org/10.2514/1.33819>.
- [57] S.L. Brunton, C.W. Rowley, D.R. Williams, Reduced-order unsteady aerodynamic models at low Reynolds numbers, *J. Fluid Mech.* 724 (2013) 203–233. <https://doi.org/10.1017/jfm.2013.163>.
- [58] M. Balajewicz, F. Nitzsche, D. Feszty, Application of Multi-Input Volterra Theory to Nonlinear Multi-Degree-of-Freedom Aerodynamic Systems, *AIAA J.* 48 (2010) 56–62. <https://doi.org/10.2514/1.38964>.
- [59] Q. Wang, W. Qian, K. He, Unsteady aerodynamic modeling at high angles of attack using support vector machines, *Chin. J. Aeronaut.* 28 (2015) 659–668. <https://doi.org/10.1016/j.cja.2015.03.010>.
- [60] D.R. Williams, F. Reißner, D. Greenblatt, H. Müller-Vahl, C. Strangfeld, Modeling Lift Hysteresis on Pitching Airfoils with a Modified Goman–Khrabrov Model, *AIAA J.* 55 (2017) 403–409. <https://doi.org/10.2514/1.J054937>.
- [61] M. Goman, A. Khrabrov, State-space representation of aerodynamic characteristics of an aircraft at high angles of attack, *J. Aircr.* 31 (1994) 1109–1115. <https://doi.org/10.2514/3.46618>.
- [62] M. Selig, Modeling Full-Envelope Aerodynamics of Small UAVs in Realtime, in: *AIAA Atmospheric Flight Mech. Conf.*, AIAA, Toronto, Canada, 2010. <https://doi.org/10.2514/6.2010-7635>.
- [63] D.R. Williams, X. An, S. Iliev, R. King, F. Reißner, Dynamic hysteresis control of lift on a pitching wing, *Exp. Fluids.* 56 (2015). <https://doi.org/10.1007/s00348-015-1982-y>.
- [64] D.M. Luchtenburg, C.W. Rowley, M.W. Lohry, L. Martinelli, R.F. Stengel, Unsteady High-Angle-of-Attack Aerodynamic Models of a Generic Jet Transport, *J. Aircr.* 52 (2015) 890–895. <https://doi.org/10.2514/1.C032976>.
- [65] R.L. Graham, D.E. Knuth, O. Patashnik, *Concrete mathematics: a foundation for computer science*, Addison-Wesley, Reading, MA, 1994.
- [66] X. An, D.R. Williams, J. Eldredge, T. Colonius, Modeling Dynamic Lift Response to Actuation, in: *54th AIAA Aerosp. Sci. Meeting*, AIAA, San Diego, CA, 2016. <https://doi.org/10.2514/6.2016-0058>.
- [67] Y. Fan, Identification of an Unsteady Aerodynamic Model up to High Angle of Attack Regime, PhD Thesis, Virginia Polytechnic Institute and State University, 1997.

- [68] D. Greenblatt, H. Mueller-Vahl, D.R. Williams, F. Reissner, Goman-Khrabrov Model on a Pitching Airfoil with Flow Control, in: 8th AIAA Flow Control Conf., AIAA, Washington, DC, 2016. <https://doi.org/10.2514/6.2016-4240>.
- [69] F. Niel, Modeling and control of a wing at low Reynolds number with high amplitude aeroelastic oscillations, PhD Thesis, University of Toulouse, 2018.
- [70] T. Witelski, M. Bowen, Fast/slow Dynamical Systems, in: *Methods Math. Model.*, Springer, Cham, Switzerland, 2015: pp. 201–213. https://doi.org/10.1007/978-3-319-23042-9_10.
- [71] R.L. Bisplinghoff, H. Ashley, R.L. Halfman, *Aeroelasticity*, Addison-Wesley, Reading, MA, 1957.
- [72] V.C. Sherrer, T.J. Hertz, M.H. Shirk, Wind Tunnel Demonstration of Aeroelastic Tailoring Applied to Forward Swept Wings, *J. Aircr.* 18 (1981) 976–983. <https://doi.org/10.2514/3.57589>.
- [73] A. Attaran, D.L. Majid, S. Basri, A.S. Mohd Rafie, E.J. Abdullah, Structural optimization of an aeroelastically tailored composite flat plate made of woven fiberglass/epoxy, *Aerosp. Sci. Technol.* 15 (2011) 393–401. <https://doi.org/10.1016/j.ast.2010.09.005>.
- [74] G. Xu, G. Liu, X. Jiang, W. Qian, Effect of pitch down motion on the vortex reformation over fighter aircraft, *Aerosp. Sci. Technol.* 73 (2018) 278–288. <https://doi.org/10.1016/j.ast.2017.12.006>.
- [75] B.-F. Ma, X.-Y. Deng, Z. Rong, B. Wang, The self-excited rolling oscillations induced by fore-body vortices, *Aerosp. Sci. Technol.* 47 (2015) 299–313. <https://doi.org/10.1016/j.ast.2015.10.003>.
- [76] L.E. Ericsson, M.E. Beyers, Forebody Flow Control at Conditions of Naturally Occurring Separation Asymmetry, *J. Aircr.* 39 (2002) 252–261. <https://doi.org/10.2514/2.2946>.
- [77] J.E. Bernhardt, D.R. Williams, Proportional Control of Asymmetric Forebody Vortices, *AIAA J.* 36 (1998) 2087–2093. <https://doi.org/10.2514/2.310>.
- [78] L. Cohen, *Time-frequency analysis*, Prentice Hall, Englewood Cliffs, NJ, 1995.
- [79] L. Durak, O. Arikan, Short-time fourier transform: two fundamental properties and an optimal implementation, *IEEE Trans. Signal Process.* 51 (2003) 1231–1242. <https://doi.org/10.1109/TSP.2003.810293>.
- [80] T. Liu, J. Huang, S. Yan, F. Guo, Extraction and analysis of transient signals of a deployable structure vibration based on the sparse decomposition with mixed norms, *Aerosp. Sci. Technol.* 105 (2020) 106064. <https://doi.org/10.1016/j.ast.2020.106064>.